Soils and Rocks
www.soilsandrocks.com
An International Journal of Geotechnical and Geoenvironmental Engineering
ISSN 1980-9743
ISSN-e 2675-5475

Experimental, numerical, and analytical investigation of the effect of compaction-induced stress on the behavior of reinforced soil walls

Seyed H. Mirmoradi[1,#], Maurício Ehrlich[1], Gabriel Nascimento[2]

Article

Keywords
Compaction
Design method
Experimental study
Numerical analysis
Reinforced soil walls

Abstract
The influence of the compaction-induced stress (CIS) is experimentally, numerically and analytically evaluated on the behavior of reinforced soil walls (RSWs), under working stress conditions. Experimental studies have been carried out to evaluate the effect of the compaction condition at the back of the block facing on the behavior of geosynthetic-reinforced soil walls using three large-scale geosynthetic-reinforced soil walls constructed at the COPPE/UFRJ Geotechnical Laboratory. The numerical analyses have been carried out using the two-dimensional finite difference computer program FLAC to verify the influence of the compaction modelling procedure at the end of construction as well as post-construction performance of a full-scale geosynthetic-reinforced soil, GRS, segmental wall under surcharge loading. Two procedures for modelling the CIS found in the literature were employed in the analyses. Moreover, the calculated values using two design methods have been compared to the measurements and numerically calculated maximum reinforcement load, T_{max}, to evaluate the prediction accuracy of these methods when the value of the CIS is relevant.

1. Introduction

The effect of backfill compaction on the behavior of reinforced soil (RS) walls has been investigated and discussed in some studies found in the literature (*e.g.*, Ehrlich & Mitchell, 1995, Tatsuoka *et al.*, 1997, Uchimura *et al.*, 2003, Ehrlich *et al.*, 2012, Ehrlich & Mirmoradi, 2016). Depending on the magnitude of the compaction-induced stress (CIS) and the wall height, the horizontal residual stresses in the reinforced soil mass may be much greater than those from a geostatic origin, which may lead to a significant increase in the reinforcement loads. This effect is also dependent on the soil type, because higher interlocking may lead to greater induced stress due to backfill compaction. As a result, the structure becomes less sensitive to post-construction movements. The final effect of this process can be understood as a kind of over-consolidation or pre-loading of the reinforced soil mass that may significantly reduce post-construction movements (Ehrlich & Mitchell, 1995, Ehrlich *et al.*, 2012).

Depending on some controlling factors such as wall height, backfill material, facing, reinforcement and foundation stiffness, CIS may significantly affect the connection load values, which may be strongly influenced by the differential settlement (Ehrlich *et al.*, 2012). A review of case studies carried out by Koerner & Koerner (2013, 2018) including 320 failed mechanically stabilized earth (MSE) walls has shown that 72 % of the failure case histories had poor or moderate compaction, which emphasized the influence of this factor on the wall performance. For the backfill soil, it is recommended to achieve 95 % standard Proctor compaction (Berg *et al.*, 2009, Collin *et al.*, 2002, Bernardi *et al.*, 2009, Koerner & Koerner, 2013).

Furthermore, regarding compaction conditions of the backfill near the facing, some recommendations have been made, such as using lightweight compaction equipment (recommended by the Federal Highway Administration, FHWA) or placing higher quality backfill in this zone to obtain the desired properties with reduced compaction effort in order to minimize the compaction-induced outward deformation and lateral stresses against the back of the facing. The application of heavy compaction equipment may also cause structural damage of the wall facing. Neverthe-

[#]Corresponding author. E-mail address: shm@ufrj.br.
[1]Programa de Engenharia Civil, COPPE, Universidade Federal do Rio de Janeiro, Rio de Janeiro, RJ, Brazil.
[2]Departamento de Engenharia Agrícola e Meio Ambiente, Universidade Federal Fluminense, Niterói, RJ, Brazil.

Submitted on June 1, 2020; Final Acceptance on July 9, 2020; Discussion open until December 31, 2020.
DOI: https://doi.org/10.28927/SR.433419

less, it should be noted that this zone is an important part of the backfill from a structural standpoint and may have a significant effect on the wall response, such as wall deformation and reinforcement strains (Hatami *et al.*, 2008).

Most of the current design methods, which are limit equilibrium (LE) methods or are based on the Rankine method, do not explicitly take into account the effect of the CIS on their calculations. Examples are the AASHTO (2017) method in the USA and the BS 8006 (BSI, 2010) method in the UK. This deficiency may be overcome by using the analytical method proposed by Mirmoradi & Ehrlich (2015a) that included the effect of CIS to use with any conventional design methods that do not already take into consideration the effect of CIS in calculations. Nevertheless, these methods have also some other important drawbacks. For example, these methods disregard the effects of reinforcement deformability, soil deformability, and in some cases cohesion. Working stress design methods have been developed to overcome these deficiencies and address more realistic approaches to the complex behaviour of reinforced soil structures (*e.g.*, Ehrlich & Mitchell, 1994, Ehrlich & Mirmoradi, 2016). The Ehrlich & Mitchell (1994) method and the simplified version of this method proposed by Ehrlich & Mirmoradi (2016) explicitly consider the effect of compaction in the determination of the maximum tensile force in the reinforcements, T_{max}.

Regarding the numerical simulation, it should be notice that if boundary conditions, geometry, constitutive models, parameters, and representative modelling procedure are correctly employed, numerical modelling may be a powerful tool to properly represent field conditions. Over the last few decades, several numerical studies have been carried out to investigate the influence of different controlling factors including the compaction effort on the behaviour of reinforced soil structures (*e.g.*, Hatami & Bathurst, 2005, Guler *et al.*, 2007, Ambauen *et al.*, 2015, Mirmoradi & Ehrlich, 2015b, Scotland *et al.*, 2016, Zheng & Fox, 2017, Zheng *et al.*, 2018, Jiang *et al.*, 2019). In the studies in which CIS was modelled, two procedures have been used (hereafter referred to as procedures type I and type II):

Type I) a uniform vertical stress applied only to the top of each backfill layer, as the wall was modelled from the bottom up (*e.g.* Hatami & Bathurst, 2005, Guler *et al.*, 2007, Ambauen *et al.*, 2015, Yu *et al.*, 2016).

Type II) an equally distributed load at the top and bottom of each soil layer (*e.g.* Mirmoradi & Ehrlich, 2015a, 2018a, Liu *et al.*, 2017, Scotland *et al.*, 2016).

Mirmoradi & Ehrlich (2014a, 2015a) stated that a model of compaction procedure type II could properly simulate the effects of compaction observed in the physical model studies. Moreover, a model of compaction procedure type I overestimated the measurements, and the discrepancy increased with depth and magnitude of the compaction effort. Nevertheless, Yu *et al.* (2016) stated that "there is no obvious advantage of one method over the other on theoretical grounds".

The present study experimentally, numerically and analytically investigates the influence of compaction-induced stress in the reinforced wall performance. The experimental study consists in the testing of large-scale geosynthetic-reinforced soil walls constructed at the COPPE/UFRJ Geotechnical Laboratory (Mirmoradi & Ehrlich, 2018b). The numerical analysis is carried out using the two-dimensional (2D) finite difference (FD) computer program FLAC. The numerical simulation of the compaction was performed using the two mentioned procedures found in the literature. The behaviour of the wall was studied using both compaction procedures at the end of construction as well as the post-construction (Nascimento *et al.*, 2020). Furthermore, two design methods are used to evaluate the prediction accuracy of these methods, when the induced stress due to the compaction is relevant (Mirmoradi & Ehrlich, 2015b, Ehrlich & Mirmoradi, 2016, Ehrlich *et al.*, 2017).

2. Experimental study

2.1 Test characteristics and material used

A series of well-instrumented physical model walls were constructed at the COPPE/UFRJ Laboratory of Physical Models. The results of two of these walls in addition to another recently constructed wall are used in this paper to evaluate the effect of compaction near the facing on the behavior of GRS walls. The three walls described here are identified as Walls 1, 2, and 3.

A cross-section of a physical model is shown in Fig. 1. The height of each physical model wall was 1.2 m. The length and vertical spacing of the geogrid were 2.2 and 0.4 m, respectively. A flexible polyester geogrid was used as reinforcement. Precast blocks were used for the wall with block facing. The walls were constructed with the facing having an inclination value of 6° to the vertical. The characteristics of the geogrid provided by the production company are shown in Table 1.

Moreover, regarding the reinforcement length it should be mentioned that in the laboratory test model the length of reinforcement was designed in order to guarantee no pullout of reinforcement from the resistant zone. Note that, as discussed by Ehrlich & Mirmoradi (2013) the value of maximum tension in the reinforcement may be consid-

Table 1. Mechanical and physical properties of reinforcement.

Longitudinal tensile strength (kN/m)	≥ 55
Transverse tensile strength (kN/m)	≥ 25
Elongation (%)	≤ 6
Weight (g/m^2)	240
Opening size (mm)	20 × 30

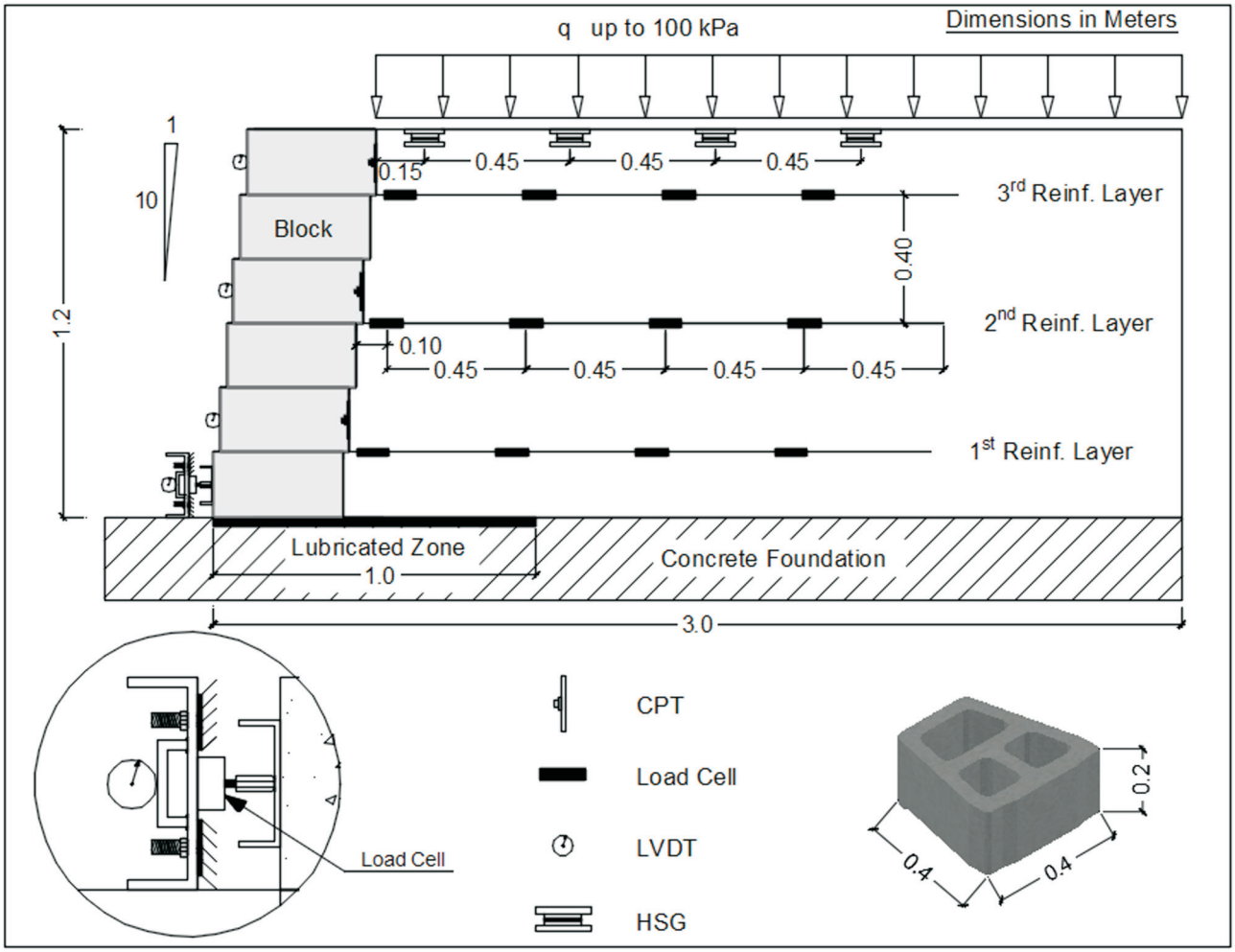

Figure 1. A cross-sectional view of a block face wall.

ered independent of the reinforcement length if there is enough length to guarantee no pullout failure. Furthermore, based on the AASHTO (2017) specification for RSWs, a minimum reinforcement length of 1.9-2.4 m, regardless of wall height, has been recommended.

The backfill material consists of well-graded sand, composed of crushed quartz powder with a significant amount of fines (19 % < #200), D_{50} = 0.25 mm, curvature coefficient C_c = 1, uniformity coefficient C_u = 8.9, and plasticity index *PI* equal to zero. Figure 2 shows the particle size distribution curve for the sand backfill.

In Wall 1, the entire surface of the backfill layers was compacted using a light vibrating plate (Dynapac LF 81) only. In Wall 2, first the entire surface of the backfill layers was compacted using a light vibrating plate, and then the backfill, except for 0.5 m from the back of the facing, was compacted using a vibratory tamper (Dynapac LC 71-ET). For Wall 3, the entire surface of the backfill layers was compacted using the vibrating plate and vibratory tamper. The equivalent static load of each compactor was determined through Kyowa accelerometers installed in the bodies of the compactors. In this case, the concept of equivalent static weight is the one presented by Ehrlich & Mitchell (1994), rather than the classic definition related to the work carried out by a force. The mass and the contact areas of the

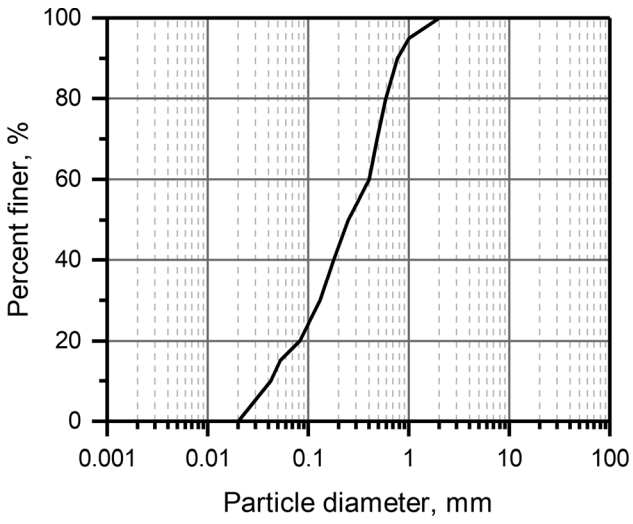

Figure 2. Grain-size curves for backfill soil.

two equipments are known and the related forces were determined through the acceleration measurements. Using this procedure, an equivalent vertical stress of 8.0 kPa was obtained by the vibrating plate (hereafter referred to as the "light compactor"), while 73 kPa was obtained by the vibratory tamper (hereafter referred to as the "heavy compactor"). Nevertheless, based on the back-analysis performed by Ehrlich *et al.* (2012), an equivalent vertical stress of 63 kPa may be obtained by the vibratory tamper.

The soil unit weights after light and heavy compactions were 19 and 20 kN/m^3, respectively and the corresponding relative density (D_r) were 71 and 89 %. The soil friction angles, considering the measured unit weight, were determined by triaxial and plane strain compression tests as 42° and 50°, respectively. Additional information about properties of the backfill soil can be found in Ehrlich *et al.* (2012), Ehrlich & Mirmoradi (2013), Mirmoradi & Ehrlich (2016) and Mirmoradi *et al.* (2016).

The toes of the block facing of the walls were restricted during the construction and surcharge application. Figure 1 also shows a schematic view of the procedure used to guarantee the toe restraint of the walls. Lateral movement of the toe was restricted by a steel beam that was fixed to the concrete U-shaped wall box using two bolts in each side of the beam (see Fig. 3).

2.2 Construction sequence and surcharge loading

The construction of the model was performed in six soil layers, 0.2 m thick and placed dry. The sequence of construction of Wall 1 was developed in two stages per layer of soil: (1) soil placement and (2) compaction of the placed backfill using the vibrating plate. In Walls 2 and 3, in addition to the two stages performed for Wall 1, a third stage was performed that entailed compaction of the backfill layer using a vibratory tamper.

The 1 m wide zone at the bottom of the walls that included the base of the block face was lubricated (sandwich of rubber sheets and Teflon grease). To reduce the effect of the lateral friction at the interface between the backfill soil and the concrete wall, PVC sheets were installed in all lateral faces of the wall that comprise the U-shaped concrete box of the model. In addition, in order to assure a plane strain condition during the tests, a thin layer of Teflon grease covered by PVC and plastic sheets were used to minimize the friction between the soil and the model box. The friction angle between the rubber sheets and the Teflon grease was measured about 3°. Moreover, the concrete box used to perform the physical model tests was designed to make possible the assumption of no normal strain in the transversal direction of the model walls.

Three layers of reinforcement were installed along the height of the wall, placed at: 0.2 m (first layer), 0.6 m (second layer), and 1.0 m (third layer) above the bottom of the wall. Each reinforcement layer was longitudinally divided into three sections, and only the 0.5 m reinforcement placed at the center of the wall was instrumented. After the end of construction, a surcharge loading of up to 100 kPa was applied over the entire surface of the backfill soil using an air bag. The surcharge load was then kept constant at 100 kPa. In the meantime, the toes of the walls were gradually released to the free base condition at the end of the toe release (0.5 mm release in each step).

(a) (b)

Figure 3. Views of Wall 3 at the end of construction (a) and load cells installed to measure the toe horizontal load (b).

2.3 Instrumentation

The walls were instrumented to monitor the values of the reinforcement load, toe horizontal load, horizontal facing displacement, horizontal stress on the back of the block facing, and vertical displacement at the top of the walls. Reinforcement loads were monitored using the load cells installed at four points along the reinforcement (*i.e.* two load cells at each point). The load cells allowed for reinforcement load monitoring without the need to determine the reinforcement stress-strain curves, which are time dependent. The load cells were also capable of counterbalancing the temperature effects and bending moments and were strong enough to resist the stress induced during the operation of the compaction equipment (Ehrlich *et al.*, 2012, Ehrlich & Mirmoradi, 2013, Mirmoradi & Ehrlich, 2014b, Mirmoradi *et al.*, 2016).

The horizontal displacements of the wall face were monitored by LVDTs. The horizontal facing displacements were measured at the second (0.3 m height), fourth (0.7 m height), and sixth (1.1 m height) layers. Furthermore, the horizontal stress at the back of the block facing was monitored using total stress pressure cells (TPCs). Two TPCs were installed on the back of the blocks to evaluate the horizontal stress values at the top and bottom of the back of the block face. Those blocks were placed next to the second and sixth soil layers.

The toe horizontal load was measured using the load cells installed on the steel beam fixed to the concrete U-shaped wall box. The load cells were placed between the aforementioned steel beam and another steel beam installed on the blocks of the first layer. As stated earlier, a 1-m wide zone at the bottom of the walls that included the base of the block face was lubricated. Thus, the toe was free and the restriction of lateral movements was guaranteed through the load cells; the toe horizontal load was measured using these load cells (see Fig. 3).

A special device was used for monitoring the vertical displacements. This hydraulic settlement gage (HSG) consists of an acrylic settlement cell filled with mercury connected to a plastic tube, also filled with mercury, which is monitored by a pressure transducer. Any settlement or heave in the settlement cell can thus be related to the readings in the pressure transducer. For all walls, the monitoring points, HSG 1, HSG 2, HSG 3, and HSG 4, were located at four different distances from the back of the face: 0.15, 0.6, 1.05, and 1.50 m, respectively. These instruments were installed at the top of the walls and monitored the settlement after the end of construction.

2.4 Test results

Figure 4 shows the comparison of the toe horizontal loads observed at the end of construction during application of the surcharge and during toe release for Walls 1, 2, and 3. The results show higher toe horizontal loads for the walls in which heavy compaction was applied (Walls 2 and 3). At the end of construction, the toe horizontal loads for Walls 2 and 3, respectively, are about 2.9 and 2.4 times higher than the value measured for Wall 1. At the end of loading, that is, at 100 kPa, the ratios decrease to about 1.5 and 1.4, respectively. Figure 4 also indicates the toe horizontal loads during toe release of the walls. As shown, the toe horizontal loads gradually decrease during toe releases of the walls. The toes of the Walls 1, 2, and 3 were completely released after 5, 7, and 8.5 mm, respectively.

Figure 5 presents the toe horizontal load increments during stage construction for the walls. It is shown that, irrespective of the type of the compaction used for construc-

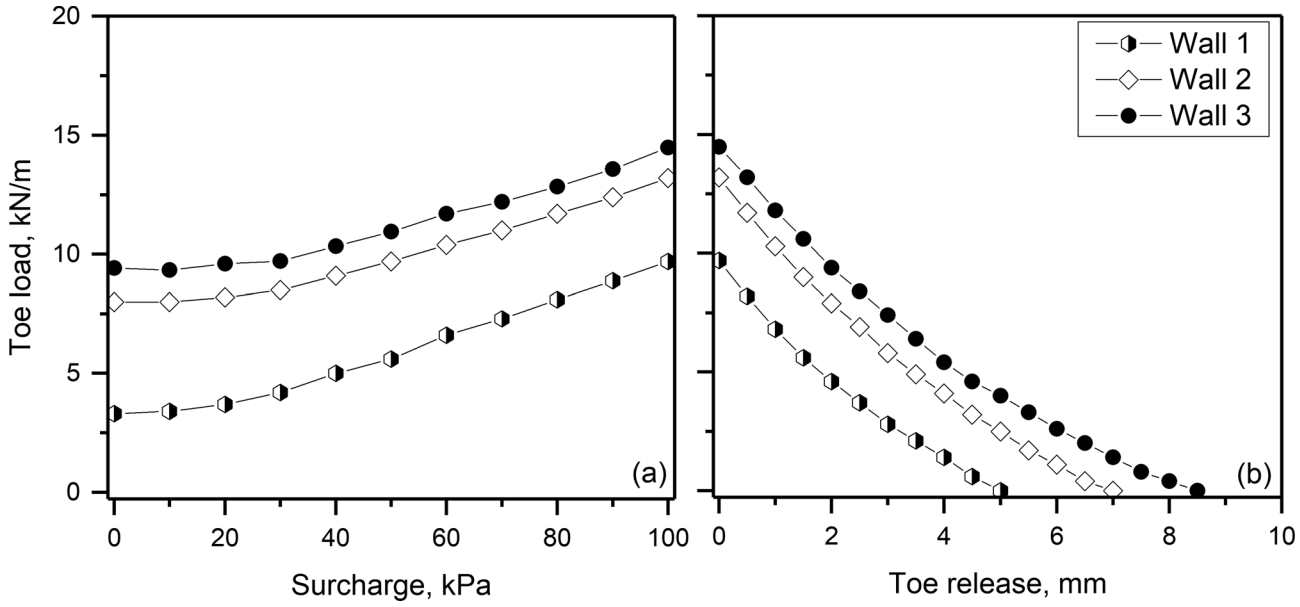

Figure 4. Toe horizontal load *vs.* surcharge application and toe release for Walls 1, 2, and 3.

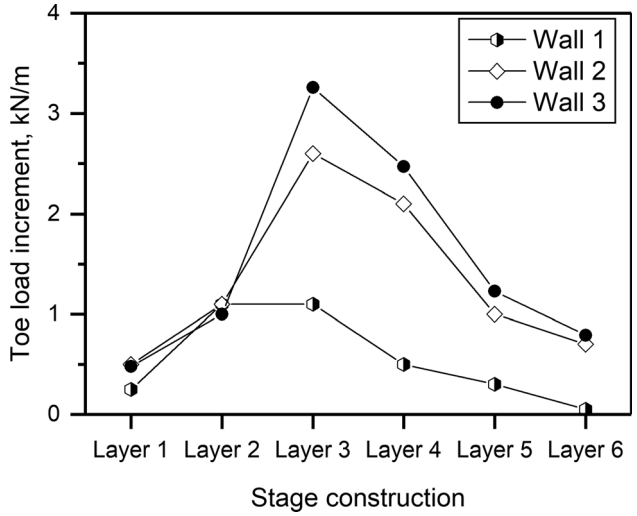

Figure 5. Toe horizontal load during construction.

tion of the walls, the maximum toe horizontal load increment occurs at the end of the construction of the third layer. Thereafter, the effect of the compaction on the toe horizontal load decreases significantly. It may be expected that after a few more layers the effect of the compaction on the increment in toe horizontal load values may disappear, in agreement with the results of the numerical analyses presented by Mirmoradi & Ehrlich (2015b).

Figure 6 shows the sum of the maximum reinforcement loads, ΣT_{max}, at the end of construction (EOC), during surcharge application and toe release. The figure indicates that although the values of ΣT_{max} are different at the EOC, this difference decreases as the applied surcharge increases and at the end of loading (EOL) similar values were measured for all walls irrespective of the compaction conditions, which agrees with the discussion presented by Ehrlich & Mitchell (1994) and Ehrlich *et al.* (2012). They stated that compaction of backfill using heavy compaction equipment may lead to a significant increase in the reinforcement load and this increase may vanish when the surcharge value exceeds the corresponding value of the vertical stress induced by heavy compaction. Figure 6(b) also illustrates that ΣT_{max} increases for the walls during toe release. Nevertheless, this increase is greater for the walls in which the backfills were compacted using light and heavy compactor equipment.

Figure 7 illustrates the measured values of the horizontal displacements during construction (Fig. 7a) and the average of the post-construction horizontal displacements (H_{ave}) *vs.* surcharge application (Fig. 7b). The figure shows that in Wall 3, in which the entire surface of the backfill was compacted using the vibratory tamper, the highest and lowest horizontal facing displacement occur during construction and post-construction, respectively. This is an expected behavior as the heavy compaction promotes displacement during the construction period and reduces post-construction horizontal displacement. This means that heavy compaction may cause the reinforced soil mass to exhibit a kind of over-consolidation that promotes a stiffer behavior after construction (Ehrlich & Mitchell, 1994, Ehrlich *et al.*, 2012, Mirmoradi & Ehrlich, 2018b). Nevertheless, this behavior is not observed for Wall 2.

Furthermore, Fig. 7 indicates that both during construction and the post-construction horizontal displacement in Wall 2 are higher than that in Wall 1. This is also observed in Fig. 8, in which the vertical displacements, measured using hydraulic settlement gage (HSG) at four positions at the end of loading and toe release, are presented.

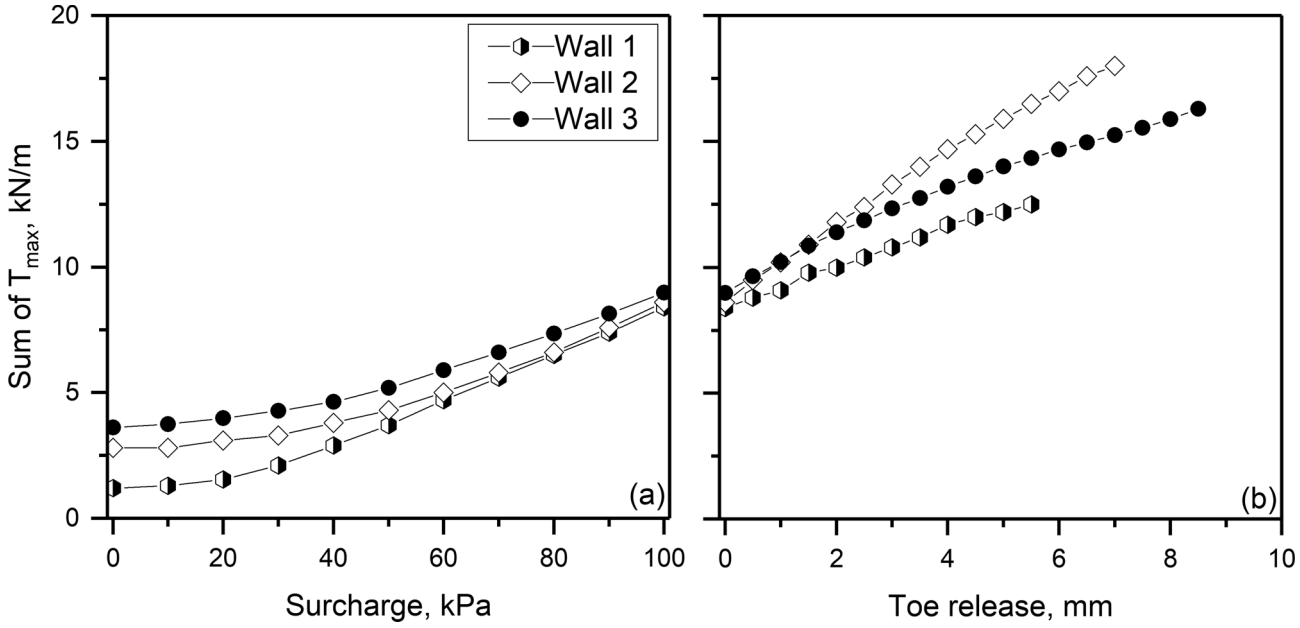

Figure 6. Sum of maximum reinforcement load (a) during surcharge application and (b) toe release.

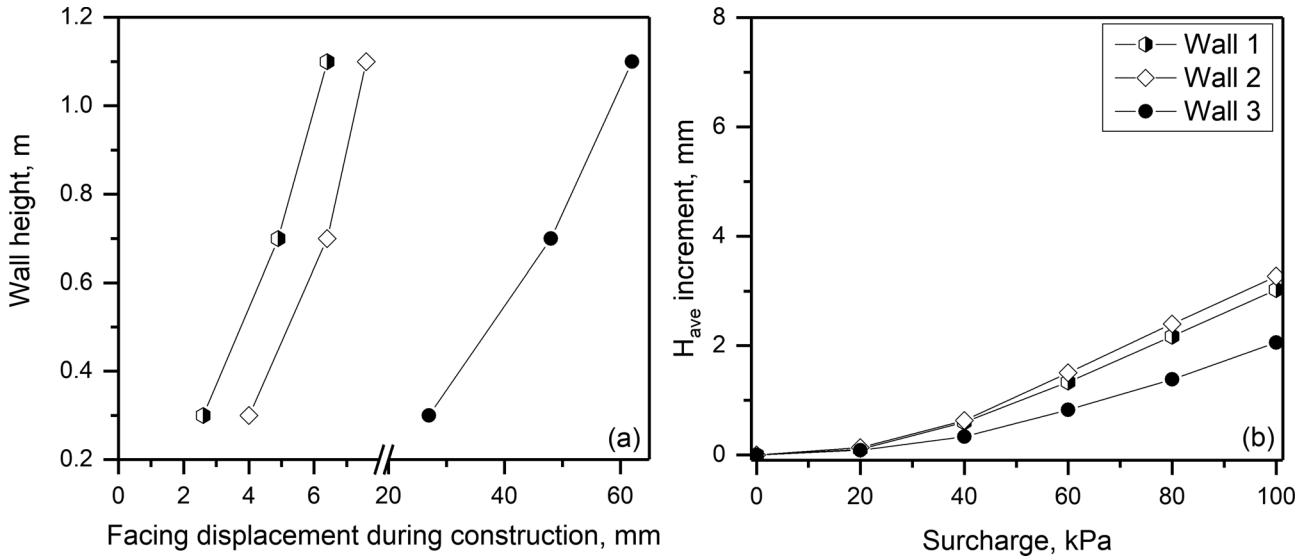

Figure 7. Horizontal facing displacement (a) during construction and (b) post construction.

The figure shows the significantly greater vertical displacements for Wall 2 in the first (0.15 m from the back of the face) and second measurement positions (0.6 m from the back of the face) compared with Walls 1 and 3. On the other hand, in the third (1.05 m from the back of the face) and fourth measurement positions (1.5 m from the back of the face), similar values were obtained for all walls. It is also indicated that the lowest vertical displacement values were measured in Wall 3 (Mirmoradi & Ehrlich, 2018b).

As stated earlier, in Wall 2, the backfill was firstly compacted with the light compactor. Then the heavy compactor was used except for the first 0.5 m of backfill directly behind the facing. The high vertical displacement of the backfill located close to the back of the facing may be associated with an increase of the void ratio of the soil near to the face due to the vibration promoted by the operation of the tamper equipment nearby. This can be clearly seen in Fig. 8, in which, the backfill soil unit weight *vs.* distance from the facing is presented for the walls. As shown, in Walls 1 and 3, the average backfill unit weights of 19 kN/m^3 and 20 kN/m^3 were measured after the end of compaction operations, irrespective of the distance from back of facing. In Wall 2 however, the magnitude of the soil unit weight measured in the first 0.5 m zone was (~5 %) lower than those measured in Wall 1, in which the same compactor equipment (light compactor) was employed in the entire

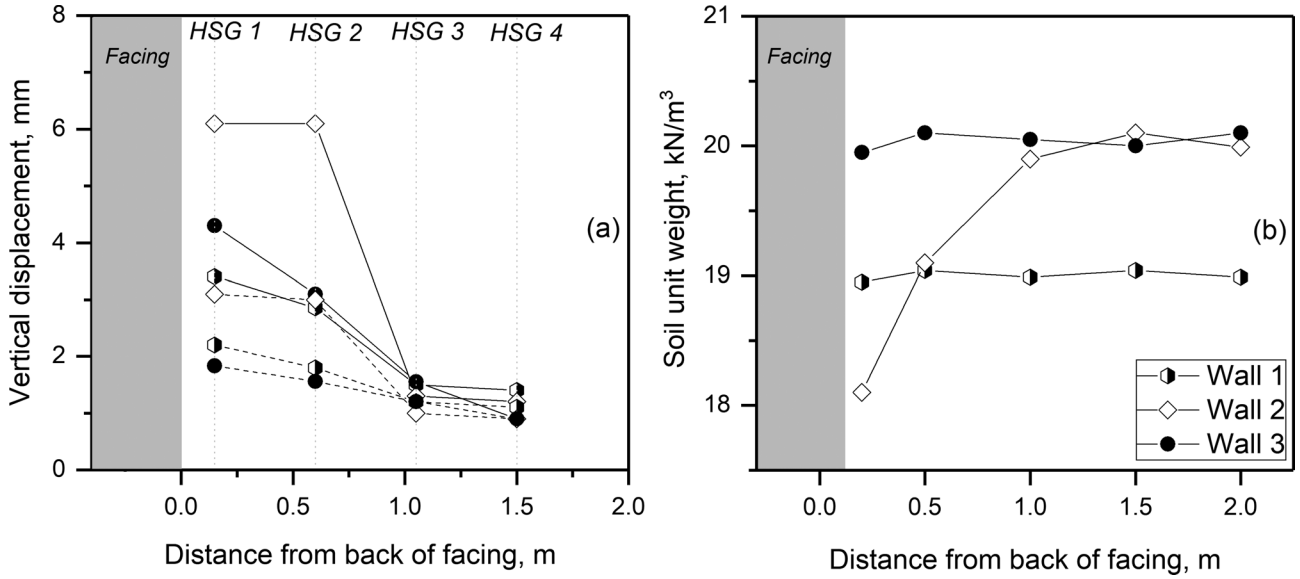

Figure 8. Vertical displacement at the end of surcharge application, EOL (dashed lines), and toe release, EOR (solid lines) and backfill soil unit weight for three walls.

surface of the soil layers. This highlights the importance of the compaction condition close to the back of the facing (Mirmoradi & Ehrlich, 2018b).

3. Numerical analysis

3.1 Compaction-induced stress

Duncan & Seed (1986) indicated that the compaction operation may be modelled by load and unload cycles that would induce high horizontal residual stresses in the soil. In the field, the soil backfill goes through a complex stress path because of the various load and unload cycles caused by the passing of compaction equipment. The roller sinks into the soil to a depth sufficient to produce a limit equilibrium condition. Note that the roller-soil contact area varies with the shear resistance and stiffness of the backfill soil that varies with the number of passes. This was simplified by Ehrlich & Mitchell (1994) by assuming only one cycle of load-unload for each layer of backfill. Note that in the modelling of compaction-induced stress-strain, soil parameters representative of the backfill soil at the end of compaction should be used, so that they represent the condition found at the last compaction cycle.

Figure 9 shows the assumed stress path due to the compaction of the backfill layer by applying a single load-unload stress cycle. In this figure, different stress states were considered, corresponding with four conditions as follows: (1) soil placement; (2) compaction equipment operation; (3) end of compaction; and (4) placement of the next soil layer. Due to the operation of the compaction equipment, the vertical stress increases to the maximum effective vertical stress induced during compaction, $\sigma'_{ZC,i}$ and simultaneously the horizontal stresses would increase to their maximum values (point 2). Although after unloading (at the end of the compaction operation) the vertical stress returns to its initial value, σ'_{Z}, (point 3), the same cannot be said to occur for the horizontal stresses, as the soil is not an elastic material. Thus, a residual horizontal stress remains in the soil due to the compaction operation ($\Delta\sigma_{SX,C}$). The placing of the next layer leads to an increase in vertical stress, and a small variation in horizontal stress (point 4). The residual horizontal stress completely disappears only when the geostatic stress at the top of the soil layer overcomes the value of the vertical stress induced during the compaction operations, $\sigma'_{ZC,i}$

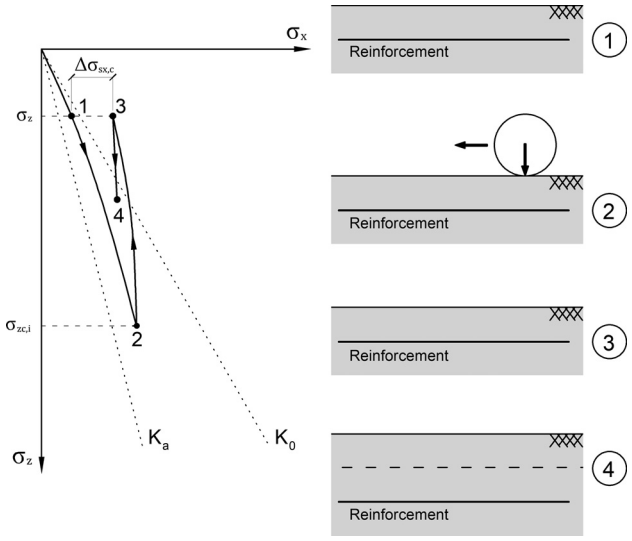

Figure 9. Assumed stress path due to compaction of soil backfill layer: (1) soil layer placement; (2) compaction equipment operation; (3) end of compaction; (4) next soil layer placement.

Figure 10 shows a schematic view of the increase in vertical stress during a roller operation in soil backfill. The vertical stress at the top of each layer during the compaction roller operation may be represented by a strip load, and an elastic solution could be used to represent its evolution with depth. For each soil layer the maximum stress increase during the roller operation occurs at the point of soil-roller contact, and decreases with depth. This depth depends on the width of the load applied for the compaction operation, *B*. For roller (strip load) and tamper (rectangular load) compactors, the depths of soil in which about 10 % of the maximum stress increase would occur during the compaction operation are about six and two times the load width, *B*, respectively (Lambe & Whitman, 1969).

Ehrlich & Mitchell (1994) stated that "in multilayer construction, the compacted layers are relatively thin, typically 0.15-0.3 m thick, and all points in each soil layer may be assumed to have been driven to the same maximum soil stress state during compaction". Therefore, it may be assumed that all points are driven to the same vertical induced stress, $\sigma'_{ZC,i}$, due to compaction.

The lateral strain of the reinforced soil layer, in the direction perpendicular to the face of the wall, reduces the maximum horizontal stress induced by compaction when compared to the maximum stress that would exist in cases

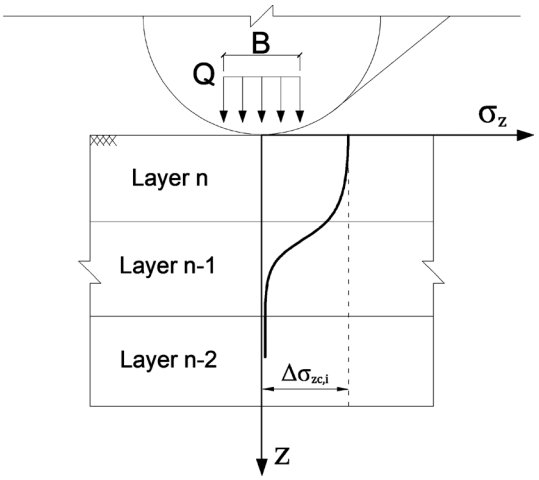

Figure 10. Vertical stress increase during a roller operation in the backfill (strip load; Boussinesq elastic solution).

where there are no lateral strains. Therefore, the actual maximum horizontal stress induced by compaction is also a function of the reinforcements and facing stiffness (point 3 in Fig. 9). However, the vertical stress induced by compaction may be assumed to be independent from the horizontal strains (Ehrlich & Mitchell, 1994).

Tables 2 and 3 show the characteristics of various vibrating rollers and vibrating tampers, respectively, which were provided by the producing companies. For plates, the vertical compaction-induced stress, $\sigma'_{ZC,i}$, can be assumed to be the average contact pressure at the base of the equipment. The centrifugal forces listed are the maximum vibration amplitude of the rollers. Figure 11 shows the $\sigma'_{ZC,i}$ values of compactor rollers for soil with a specific 18 kN/m^3 weight and various angles of friction, determined using equations developed by Ehrlich & Mitchell (1994). For a cohesionless soil, $\sigma'_{ZC,i}$ is given by:

$$\sigma'_{ZC,i} = \frac{1+K_a}{1+K_0}\left[\frac{1}{2}\gamma' Q\frac{N_\gamma}{L}\right]^{1/2} \quad (1)$$

where K_a is the Rankine active earth pressure coefficient, K_0 is the at rest earth pressure coefficient calculated using Jaky's equation (Jaky, 1944); Q is the compactor equipment equivalent static load, L is the length of the roller drum, γ' is the effective soil unit weight and N_γ is the soil-bearing capacity factor according to the Rankine wedge theory, calculated by:

$$N_\gamma = \tan(45°+\phi'/2)[\tan^4(45°+\phi'/2)-1] \quad (2)$$

where ϕ' is the effective stress friction angle. As shown in Fig. 11, the value of the induced stress due to compaction operation significantly varies with the soil backfill friction angle. The reader is directed to the paper by Ehrlich & Mitchell (1994) for details about the derivation of the equations.

3.2 Model characteristics

The physical model used for the numerical modelling validation was built at the Royal Military College of Canada (RMC), and consisted of a 3.60 m high reinforced soil

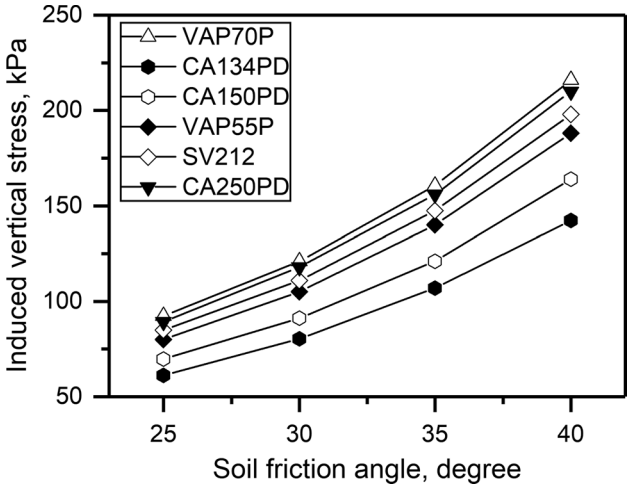

Figure 11. Vertical stress induced by several compactor rollers (after Ehrlich & Becker, 2010).

Table 2. Characteristics of various vibrating roller compactors (after Ehrlich & Becker, 2010).

Manufacturer	Model	Weight (kN)	Width (m)	Equivalent static load (kN)	Vertical stress (kPa)
Case	SV212	72.3	2.20	277	*
Müller	VAP55P	-	1.68	190	*
	VAP70P	-	2.14	320	*
Dynapac	CA134PD	19.6	1.37	89	*
	CA150PD	39.2	1.68	143	*
	CA250PD	72.6	2.13	300	*

* See Fig. 11.

Table 3. Characteristics of rammer compactors (after Ehrlich & Becker, 2010).

Manufacturer	Model	Equivalent static load (kN)	Base area (m^2)	Vertical stress (kPa)
Dynapac	LT500	10.0	0.076	132
	LT600	14.8	0.092	160
	LT700	18.6	0.092	201
Wacker	BS 50-4	14.7	0.092	159
	BS 60-4	15.6	0.092	169
	BS 70-2i	17.8	0.092	193

wall with a face inclination of 8° to the vertical. The reinforcement was provided by polypropylene (PP) geogrids with 0.60 m vertical spacing and approximately 2.20 m length (Hatami & Bathurst, 2006).

The numerical modelling was developed using the code FLAC version 8.0.455 (Itasca Consulting Group, 2016), which is based on the finite difference method (FDM). According to this method, the continuum material (*e.g.* soil and concrete) is discretized into zone regions (quadrilaterals) defined by grid points (GPs). Figure 12 shows the numerical grid used for the segmental retaining wall.

The bottom GPs (first row) of the soil regions were restrained to move in horizontal and vertical (x and y) directions, simulating a rigid foundation and a no-slip condition. At the backfill far-end boundary, the GPs were allowed to move only in the vertical direction and, at the first block, the bottom GPs were allowed to move only in the horizontal direction. A spring connected to a GP from the bottom left corner represented the load ring from the physical model, considering a 4 (MN/m)/m toe stiffness.

The mechanical connectors between the blocks and reinforcements of the physical model were numerically represented by two-node beam elements with large axial and bending stiffness. The master/slave pair FLAC feature made it possible to restrain the element nodes displacements to the corresponding nodes of the block (x and y direction) or GPs of the soil (y direction) regions. Cable elements represented the reinforcement with a nonlinear tangent stiffness, calculated by (Hatami & Bathurst, 2006).

$$J_t = \frac{1}{J_0\left(\frac{1}{J_0} + \frac{\eta}{T_f}\varepsilon\right)^2} \tag{3}$$

where J_t = time-dependent reinforcement tangent stiffness function; J_0 = initial tangent stiffness; η = scaling function; T_f = stress-rupture function for the reinforcement; ε = strain; and t = time. The parameters of this equation are summarized in Table 4.

The CHSoil constitutive model was adopted for the soil, based on a hardening/softening logic (Itasca Consulting Group, 2016). The elastic shear and bulk modulus are calculated by

$$G^e = G_{ref}\, p_{ref}\left(\frac{p'_m}{p_{ref}}\right)^n \tag{4}$$

and

$$K^e = K_{ref}\, p_{ref}\left(\frac{p'_m}{p_{ref}}\right)^m \tag{5}$$

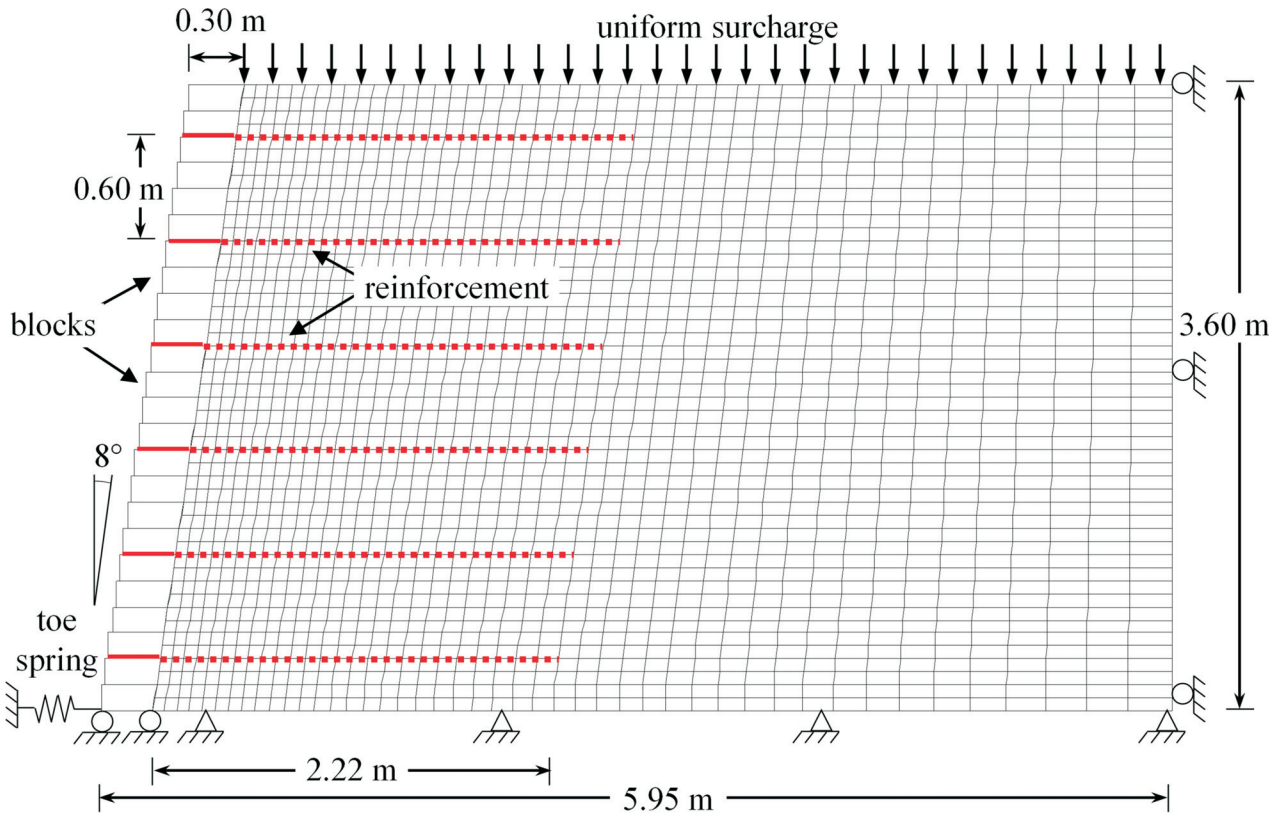

Figure 12. Numerical model grid, components and boundary conditions.

Table 4. Input parameters from the full-scale wall.

Property	Value
Soil properties	
Model	CHSoil
Friction angle, ϕ_f (°)	40 (triaxial) and 44 (plane strain)
Cohesion, c (kPa)	2.0
Ultimate dilation angle, ψ_f (°)	11.0
Unit weight, γ (kN/m^3)	16.8
Bulk modulus number, K_{ref}	575
Shear modulus number, G_{ref}	500 (triaxial) and 600 (plane strain)
Bulk modulus exponent, m	0.5
Shear modulus exponent, n	0.5
Failure ratio, R_f	0.95
Reference pressure, p_{ref} (kPa)	101.3
Min. initial mean effective pressure, p'_m (kPa)	1.0
Reinforcement	
Elastic axial stiffness (kN/m)	variable, Eq. (3)
Initial tangent stiffness, J_0 (kN/m)	115
Scaling factor, η	0.85
Rupture load, T_f (kN/m)	7.7
Modular block properties	
Model	Linear elastic
Size (m × m)	0.30 × 0.15 (length × height)
Weight (kg)	20
Stiffness modulus (GPa)	2.0
Poisson's ratio, ν	0.15
Block-block interface	
Friction angle (°)	57
Cohesion (kPa)	46
Normal stiffness, k_{nbb} (MPa/m)	1 000
Shear stiffness, k_{sbb} (MPa/m)	50
Soil-block interface	
Friction angle (°)	44
Dilation (°)	11
Normal stiffness, k_{nbb} (MPa/m)	100
Shear stiffness, k_{sbb} (MPa/m)	1
Grout (backfill-reinforcement)	
Friction angle (°)	44
Adhesive strength (kPa)	1,000
Shear stiffness [(kN/m)/m)]	1,000
Toe condition	
Axial stiffness of anchor [(kN/m)/m)]	4,000

respectively, where $p'_m = (\sigma'_1 + \sigma'_2 + \sigma'_3)/3$ is the initial value of the mean effective stress; G_{ref}, K_{ref} and p_{ref} are reference values; and m and n are constant exponents. In order to avoid an inconsistent Poisson equivalent value, K^e is limited by $2G^e/3 < K^e < 49.66G^e$.

The mobilized friction angle ϕ_m increases as a strain-hardening behaviour represented by

$$d(\sin\phi_m) = \frac{G^p}{p'_m} d(\gamma^p) \tag{6}$$

where γ^p is the plastic shear strain and the plastic shear modulus G^e is calculated by

$$G^p = G^e \left(1 - \frac{\sin\phi_m}{\sin\phi_f} R_f\right)^2 \tag{7}$$

where ϕ_f is the ultimate friction angle and R_f is the failure ratio, which assigns a lower bound to G^p.

To represent the typical dilation behaviour, the mobilized dilation angle is assumed as $\psi_m = 0$ for $\phi_m < \phi_{cv}$, then $\psi_m = \psi_f$ for $\phi_m > \phi_{cv}$, where ψ_f is the ultimate dilation angle and ϕ_{cv} is the mobilized friction angle at constant volume, estimated by

$$\sin\phi_{cv} = \frac{\sin\phi_f - \sin\psi_f}{1 - \sin\phi_f \sin\psi_f} \tag{8}$$

The values selected for the parameters (Table 4) produced a good match for the soil stress-strain curve under confining pressures equal to 20 kPa and 30 kPa, and for strain less than 1.5 % (Fig. 13), which corresponds to the stress levels during the analysis.

The same procedure and interface values employed by Huang *et al.* (2009) are used in this study. The contact between components (*i.e.* block-block and block-soil) was modelled with interface pairs based on Coulomb sliding and normal/shear stiffness (Table 4). The interaction between the reinforcement and soil is modelled by the grout feature, which provides a rigid attachment until the adhesive strength is overcome, then slipping is allowed and friction force is calculated by the friction angle and cohesion. High value of soil-reinforcement interface resistance employed in the analyses results in no slip between soil and reinforcement. As shown by Dyer & Milligan (1984) and Jewell (1980), perfect adherence is a reasonable assumption for a soil-reinforcement interface under working stress conditions.

3.3 Numerical modelling of compaction

Backfill soil placement and compaction were modelled during the stage construction. Two different procedures were used for modelling the CIS during the construction sequence (Mirmoradi & Ehrlich, 2018a):

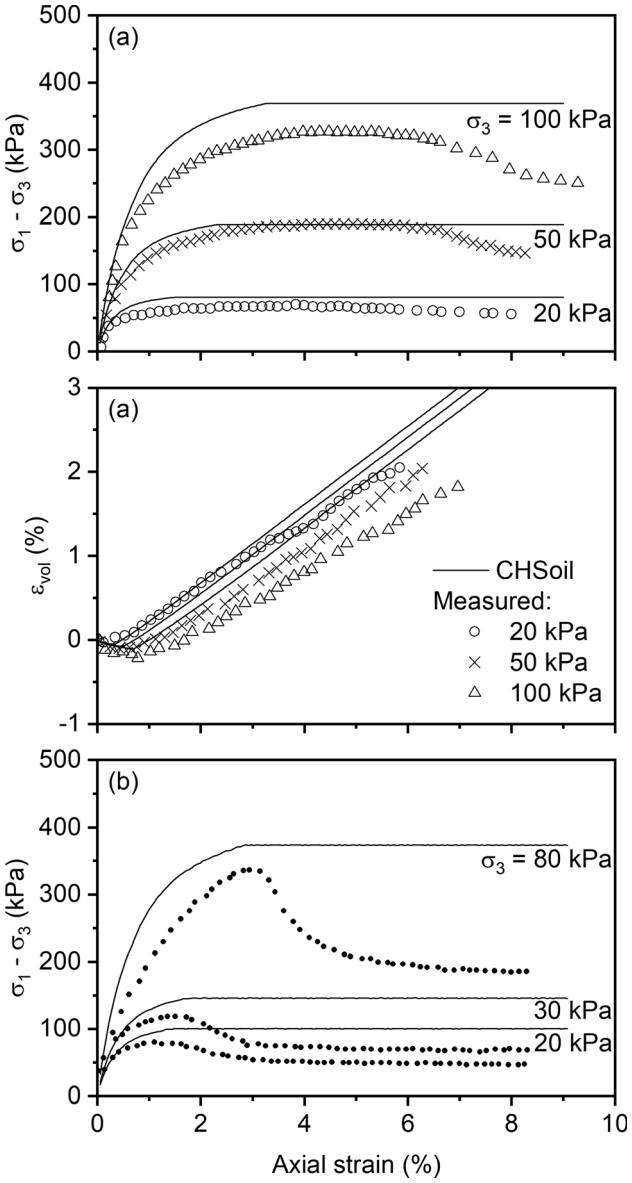

Figure 13. Soil constitutive model response compared to measured values from (a) triaxial and (b) plane strain tests presented by Hatami & Bathurst (2005).

- **Type I**: A uniform vertical stress is applied at the surface and then removed (*e.g.* Hatami & Bathurst, 2005) (referred to as procedure type I, see Fig. 14a).
- **Type II**: During the application of the vertical stress, the GPs located at the bottom of the layer are prevented from vertical displacement, which restricts the vertical stress increment to only the layer being compacted as suggested by Mirmoradi & Ehrlich (2015a) (referred to as procedure type II, see Fig. 14b). This means that during compaction of a given soil layer, no vertical stress increase takes place in the underlying layers. This approach is an adaptation of the original procedure described by the referred authors, where the vertical stress was applied to both sides (top and bottom) of each layer.

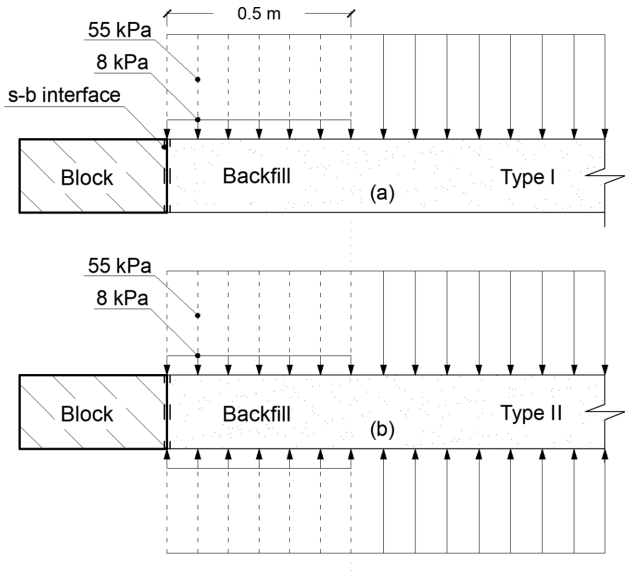

Figure 14. Compaction procedures employed in the numerical analyses.

Regarding the compaction condition of the physical model considered in this study, it should be mentioned that the first 0.5 m directly behind the wall-facing was hand-tamped to a target 95 % of standard Proctor density, using a rigid steel plate to minimise construction-induced outward deformation and lateral stresses against the back of the facing. The backfill located beyond 0.5 m of the facing was compacted in 150 mm lifts using three passes of a walk-behind, gasoline-powered, vibrating-plate compactor (Whacker VPG-155A) with a dynamic contact pressure of 55 kPa (Bathurst *et al.*, 2009).

For the numerical modelling of compaction, two conditions were considered, as shown in Fig. 14: A) The vertical stress used to model the CIS in the first 0.5 m behind the facing was 8 kPa, and the value of 55 kPa was employed for the backfill located beyond 0.5 m of the facing; B) The value of 55 kPa was applied to the entire surface of the backfill (including the first 0.5 m behind the facing). These two conditions have been considered in all the analyses using the different procedures employed for modelling CIS, *i.e.* types I and II. Note that in the physical model, the first 0.5 m directly behind the wall-facing was hand-tamped using a rigid steel plate and beyond that was compacted using a vibrating-plate (Whacker VPG-155A) with a dynamic contact pressure of 55 kPa (Bathurst *et al.*, 2009). After the end of construction, a uniform vertical stress was applied at the entire surface of the top of the wall. The vertical stress was gradually raised by increments of 0.001 kPa to 80 kPa.

Figure 15 shows two different approaches for the simulation of the induced stress due to compaction. Figures 15a and b show a schematic view of the numerical modelling of

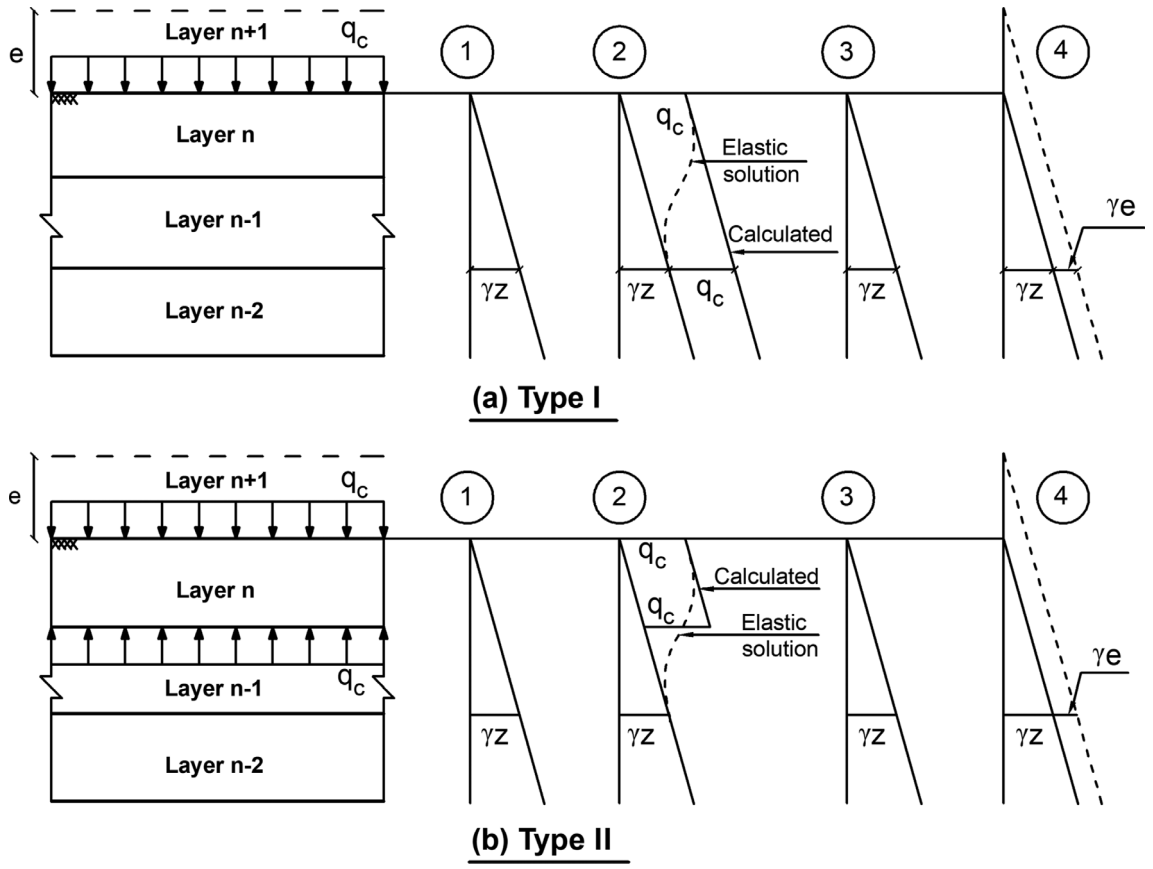

Figure 15. Modelling of the vertical stress load-unload cycles verified during the compaction of the backfill layer, using compaction procedures types I and II.

compaction-induced stress using a distributed load, q_c, at the top of each soil layer (type I); and distribution loads, q_c, at the top and bottom of each soil layer (type II), respectively. Stage construction is used in all procedures, and compaction modelling is represented by only one cycle of loading and unloading for each soil layer. In Fig. 15, four steps for backfill soil construction in a specific soil layer, n, were considered: (1) soil layer placement, (2) compaction equipment operation, (3) end of compaction, and (4) next soil layer placement (layer $n + 1$). Figure 15a, step (2) shows that when procedure type I is used for numerical modelling of the induced stresses due to compaction in soil layer n, it leads to a constant increase in the vertical stress due to compaction, q_c, in all layers below. The dashed line in this figure shows the expected vertical stress increased during the roller operation for soil layer n based on the strip load elastic solution, where its maximum value takes place at soil-roller contact and decreases significantly with depth. This figure clearly shows that using the distribution load solely at the top of each soil layer when modelling compaction cannot match the actual field conditions represented by the elastic solution.

Figure 15b shows a schematic view of procedure type II, as suggested by Ehrlich & Mirmoradi (2013) and Mirmoradi & Ehrlich (2015a) for the numerical simulation of the induced stress due to compaction. Figure 15b, step (2) shows that when procedure type II is used for the soil layer n, all points in this soil layer would be driven to the same vertical stress increase. In addition, for the soil layers placed under this layer, only geostatic stresses occur. A comparison between the curves related to the compaction modelling using procedure type II, and the dashed line represented by the elastic solution, indicates that this procedure may be more representative of the actual induced vertical stress during roller operation.

Of note, the compaction was simulated by applying a single load-unload stress cycle, which may closely represented the actual multicycle load-unload stress path during compaction (Ehrlich & Mitchell, 1994). Campanella & Vaid (1972) through laboratory tests of multicycle loading and unloading have shown that the residual stress state of a multicycle loading and unloading can be conservatively determined by using the largest virgin hysteretic stress cycle. Thus, the one hysteretic cycle assumption may be considered to be conservative; *i.e.*, the estimated horizontal stress should be an upper-bound value for the actual one.

In the analyses performed, for both type I and II procedures, the load increments were gradually applied over 20,000 steps in order to assure numerical stability.

3.4 Results and discussion

The results obtained from the numerical analysis for the different compaction modelling approaches described above are compared with the measured values presented by Holtz & Lee (2002) and Hatami & Bathurst (2005, 2006). Figure 16 shows the reinforcement strain at the end of con-

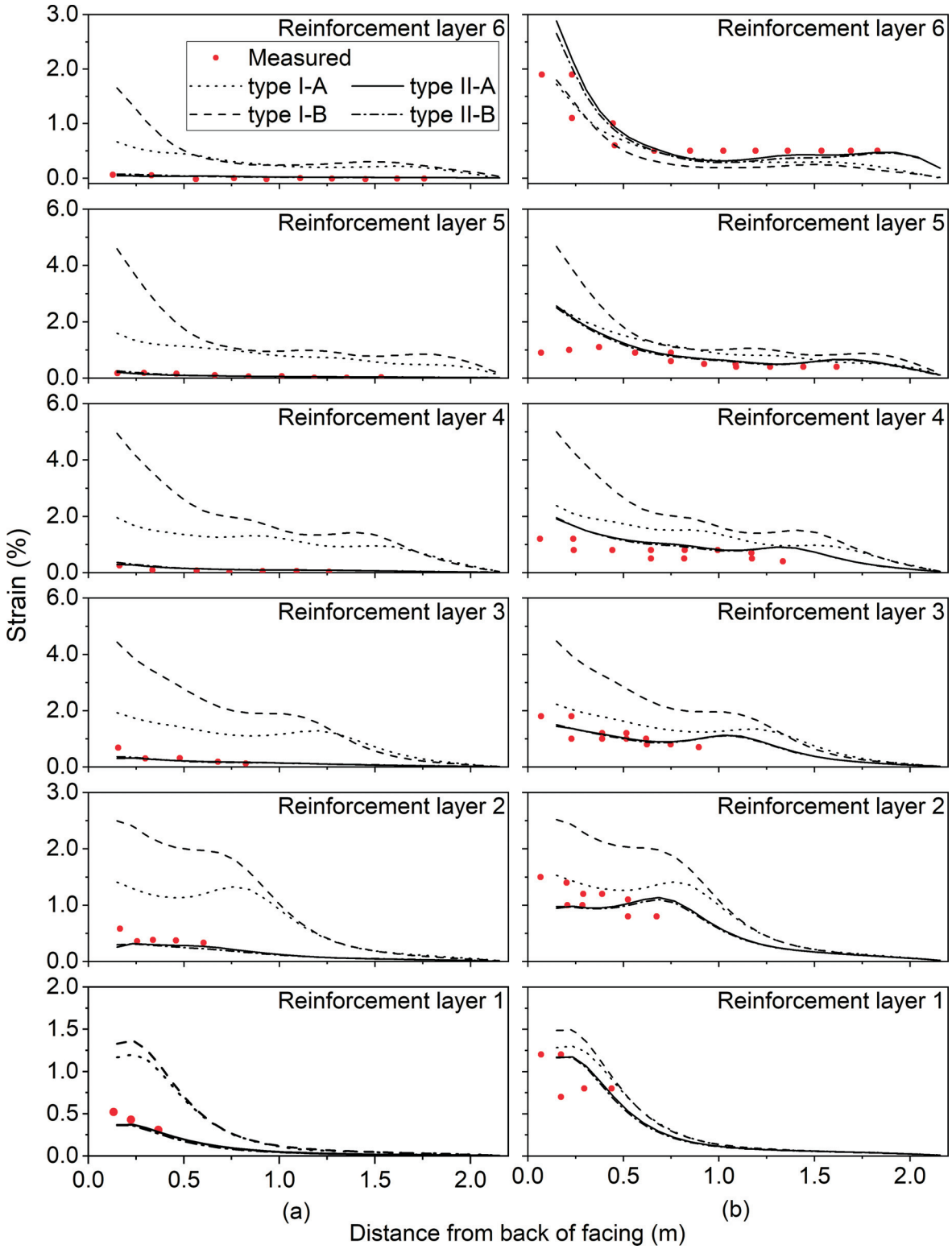

Figure 16. Measured and calculated values of reinforcement strains using different compaction modelling (a) at the end of construction and (b) under 50 kPa surcharge.

struction (EOC) and under a 50 kPa surcharge. The figure indicates that, in general, the determined values using compaction modelling type II properly represented the measurements, while the type I modelling overestimated the reinforcements strain. This agrees with the results presented by Mirmoradi & Ehrlich (2018a), who used PLAXIS 2D to simulate the same physical model wall up to the end of construction.

The connection loads calculated using type II-A and type II-B compaction modelling agree well with the measurements at EOC (Fig. 17a) and under 50 kPa surcharge (Fig. 17c). The connection loads calculated using compaction modelling type I-A & B led to overestimated values at EOC. Moreover, for 50 kPa surcharge loading and the compaction condition type I-B, the numerical model, except for the 6th reinforcement layer, over-predicted the measurements. However, when the type I-A compaction condition was considered, the results are close to the measured values. Note that the analyses performed using the type I procedure led to results that were nearly the same for EOC and during surcharge application (see Fig. 17a, b and c). On the other hand, the type II compaction modelling led to more realistic results, in which the connection load significantly increases with surcharge, as observed in the measured values obtained from the physical model wall. The discrepancy between the behaviour of the experimental models considering different compaction condition near the face and numerical analyses is related to the variation of the soil parameters. In the numerical analyses, the soil parameters used were the same, irrespective of the compaction conditions. In the physical models, however, both soil parameters and stress conditions were changed, as discussed earlier.

Figure 18 presents the measured and calculated facing horizontal displacements at each block layer during the stage construction. The displacements calculated for the modelling of compaction type I at EOC are overestimated and remain nearly constant up to 50 kPa surcharge loading, which is close to the pressure applied to model the CIS (55 kPa). The results of the numerical analyses in which the compaction type I was employed show a larger facing displacement compared with the measurement. This overestimation is more highlighted considering the lower values of the surcharge. Moreover, the shape of the facing profile is different and the maximum facing displacement did not occur at the wall top as observed in the physical model. On the other hand, the predictions using type II modelling are in good agreement with the physical model measurements, with slightly larger values determined for the model with compaction type II-B than type II-A.

The displacement calculated at the facing at 0.3 m from the toe was larger than the measurement for all conditions and types of CIS modelling. These results may indicate that the toe stiffness assumed in the numerical analyses is smaller than the real response. The value used in the present analyses was the same as that used by Hatami & Bathurst (2006), based on measurements in the physical model (4 MN/m).

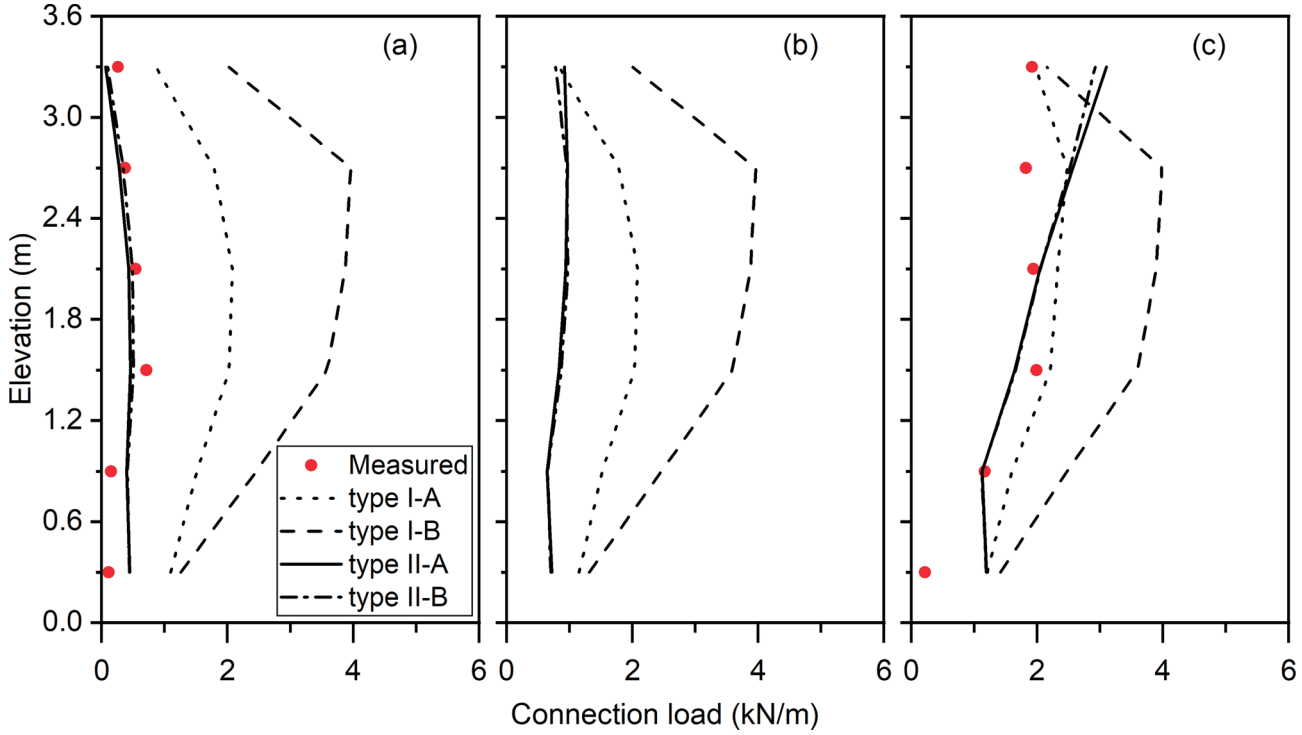

Figure 17. Measured and calculated values of connection loads using different compaction modelling (a) at the end of construction, (b) under 20 kPa and (c) 50 kPa surcharge.

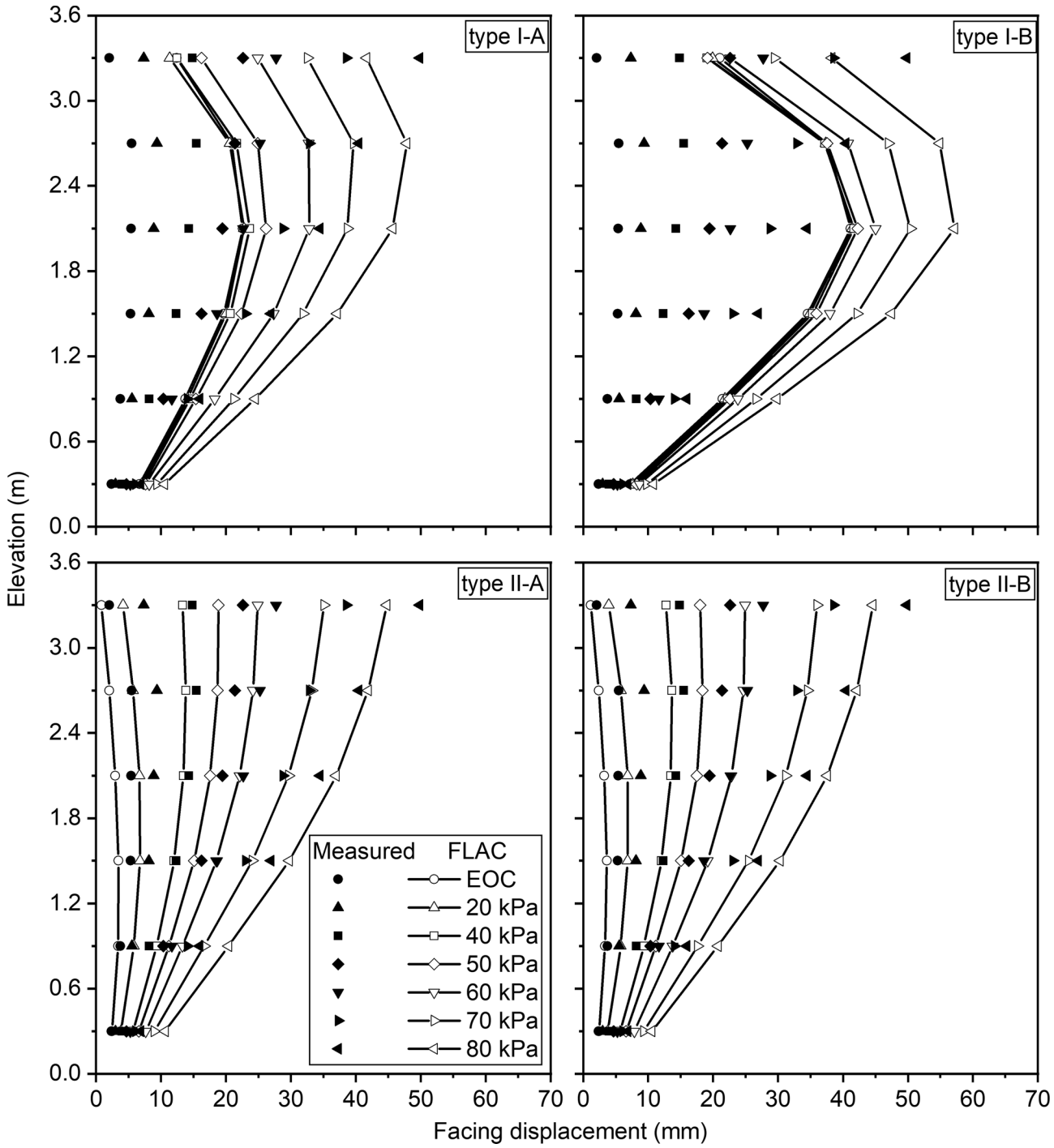

Figure 18. Measured and calculated values of the horizontal facing displacement at the end of construction (EOC) and under different surcharge loading.

Regarding the toe reaction loads during the construction, good agreement is observed between the measurements and calculated values when type II compaction modelling is used (Fig. 19a). Nevertheless, the type I modelling presented good results only for the vertical reaction and significantly overestimated the horizontal load. The determined results indicate that vertical reaction at the toe is mainly controlled by geostatic stress and is not affected by the type of modelling of the compaction induced stress. During the surcharge application, when type II modelling is used, good agreement is observed between the measured and calculated values up to 30 kPa, and then both compaction types and conditions led to larger values than the measurements (Fig. 19b).

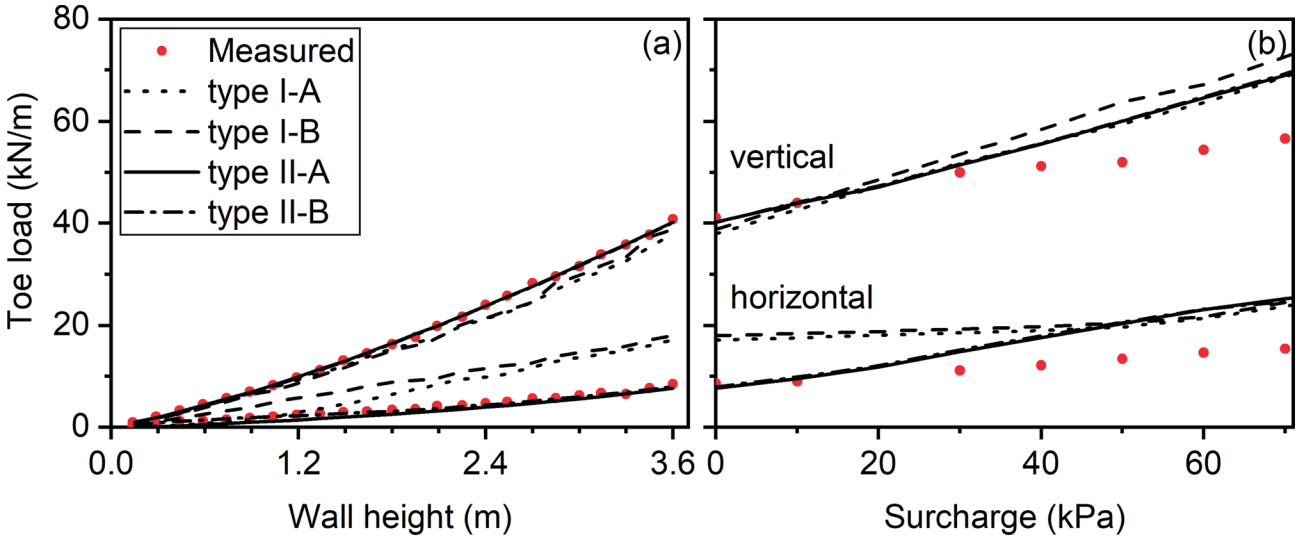

Figure 19. Measured and calculated values of the vertical and horizontal toe reactions using different compaction modelling (a) during the construction stages and (b) under different surcharge loading.

Figure 20 shows the calculated and measured values of the vertical pressure at the base of the wall. The values were normalized considering the geostatic vertical stress at that depth (soil unit weight, γ_s times wall height, H, plus surcharge, q). The results show no significant difference between the considered compaction modelling types and conditions, since, as discussed above, the geostatic stress may be the predominant controlling factor of the vertical pressure at the base of the wall.

In general, the calculated and measured normalized pressure agree and are about 1.0, except near to the face, where at 0.15 m and 0.40 m from the facing, the values were 2.2 and 0.3, and 1.6 and 0.5 for EOC and under the surcharge of 55 kPa, respectively. This behaviour is mostly due to the arching effects related to the differential vertical movements of the facing and the base of the wall.

4. Evaluation of design methods

Ehrlich & Mirmoradi (2016) proposed an analytical procedure for the calculation of T_{max} under working stress conditions. This method explicitly takes into account the effect of CIS, reinforcement and soil stiffness properties and facing inclination. The proposed method was based on Ehrlich & Mitchell's (1994) procedure. There are three key differences between the proposed method and Ehrlich & Mitchell's (1994) procedure: (1) the effect of the facing in-

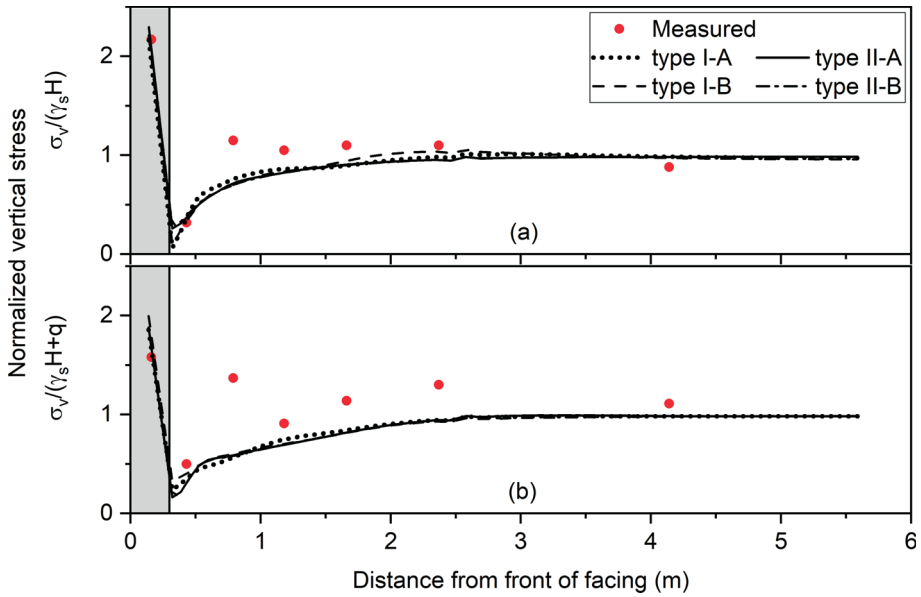

Figure 20. Measured and predicted distributions of contact pressures at the base of the wall using different compaction modelling (a) at the end of construction and (b) under 50 kPa surcharge pressure.

clination is considered in the new method, while the original method was developed for vertical walls; (2) the calculation of T_{max} using the Ehrlich & Mirmoradi (2016) method does not need iteration, which was required by the original method; and (3) the equations are simpler to use.

Furthermore, Mirmoradi & Ehrlich (2015a) proposed a new simple analytical procedure that includes the effect of the induced stress due to backfill compaction for use with conventional design methods of GRS walls. This proposed analytical procedure may be used with any conventional design methods that do not take into consideration the effect of CIS in their calculations. Of note, the currently used design methods do not explicitly take into consideration the effect of the compaction-induced stress in the calculation [e.g., AASHTO, 2017, FHWA, 2008]. Therefore, the proposed analytical method could be used to modify the calculated T_{max} using these methods to consider the effect of CIS in calculation.

In order to verify the prediction accuracy of the analytical procedures, in Fig. 21 the measured values of the summation of the maximum tension mobilized in the reinforcement provided by Ehrlich & Mirmoradi (2013), ΣT_{max}, was compared with those determined by FLAC for compaction procedures type I and II, the Ehrlich & Mirmoradi (2016) method, the AASHTO simplified method, and the modified calculated values by the AASHTO method to consider the effect of CIS, called AASHTO modified. The vertical dotted line in Fig. 21 represents the compaction influence depth, Z_c. The equivalent depth of the soil layer (Z_{eq}) is defined by:

$$Z_{eq} = Z + \frac{q}{\gamma} \quad (9)$$

where Z and q are the real depth of a specific layer and the surcharge load value of the physical model, respectively. As shown in Fig. 21, the values measured from the physical

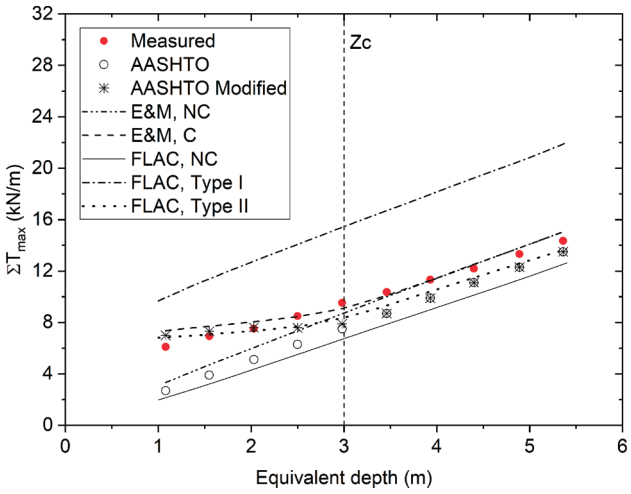

Figure 21. Comparison of measured and determined summations of the maximum reinforcement loads.

model were properly captured by the AASHTO modified method, the Ehrlich & Mirmoradi (2016) method, and the numerical analysis using compaction procedure type II. However, regardless of the value of Z_{eq}, the curve corresponding to the numerical simulation using compaction procedure type I overestimates the values of ΣT_{max} and this discrepancy increases with equivalent depth.

Comparison of the results corresponding to the conditions with and without induced stresses due to compaction illustrates that for compacted backfill soil walls, when $Z_{eq} < Z_c$, the values of ΣT_{max} are greater than the values obtained for the no-compaction conditions. However, for $Z_{eq} > Z_c$, the compaction-induced stress was overcome by the geostatic stress and the values determined are the same irrespective of whether or not the induced stress due to the backfill soil compaction is considered in the analysis.

In Fig. 21, the results related to the condition without compaction are also shown. These curves were obtained with the Ehrlich & Mirmoradi (2016) method, the AASHTO simplified method, and by numerical modeling with FLAC. The results show practically similar values for the no-compaction condition.

Figure 22 shows a comparison of the maximum mobilized tension in each reinforcement layer, T_{max}, *vs.* depth determined with FLAC for the described numerical compaction modeling (type I and II) and calculated values using the Ehrlich & Mirmoradi (2016) method and the AASHTO methods (*i.e.*, AASHTO simplified and AASHTO modified), for the compaction-induced stresses of 63 (Fig. 22a) and 120 kPa (Fig. 22b), respectively.

In Figs. 22, for the analyses in which the compaction modeling type II was used, a consistent representation of the expected behavior is found and discussed as follows. For $Z > Z_c$, the effect of compaction vanishes because the geostatic stress overcomes the induced stress due to backfill soil compaction. Furthermore, T_{max} is the same; regardless the induced stress due to backfill soil compaction is included ($Z > Z_c$). However, when $Z < Z_c$, T_{max} would be greater than the corresponding values for the no-compaction condition. Nevertheless, for the analyses in which the compaction modeling was performed using procedure type I, the T_{max} values are much larger than the previous values and this overprediction increases with depth. Good correspondence is also observed for the determined results using the AASHTO modified method and the Ehrlich & Mirmoradi (2016) method.

5. Conclusions

The present study experimentally, numerically and analytically investigated the effect of the compaction-induced stress on the behavior of GRS walls. The experimental evaluation was performed using three large-scale GRS walls with different compaction condition at the back of block facing constructed at the COPPE/UFRJ Geotechnical Laboratory. The numerical analyses were carried out using

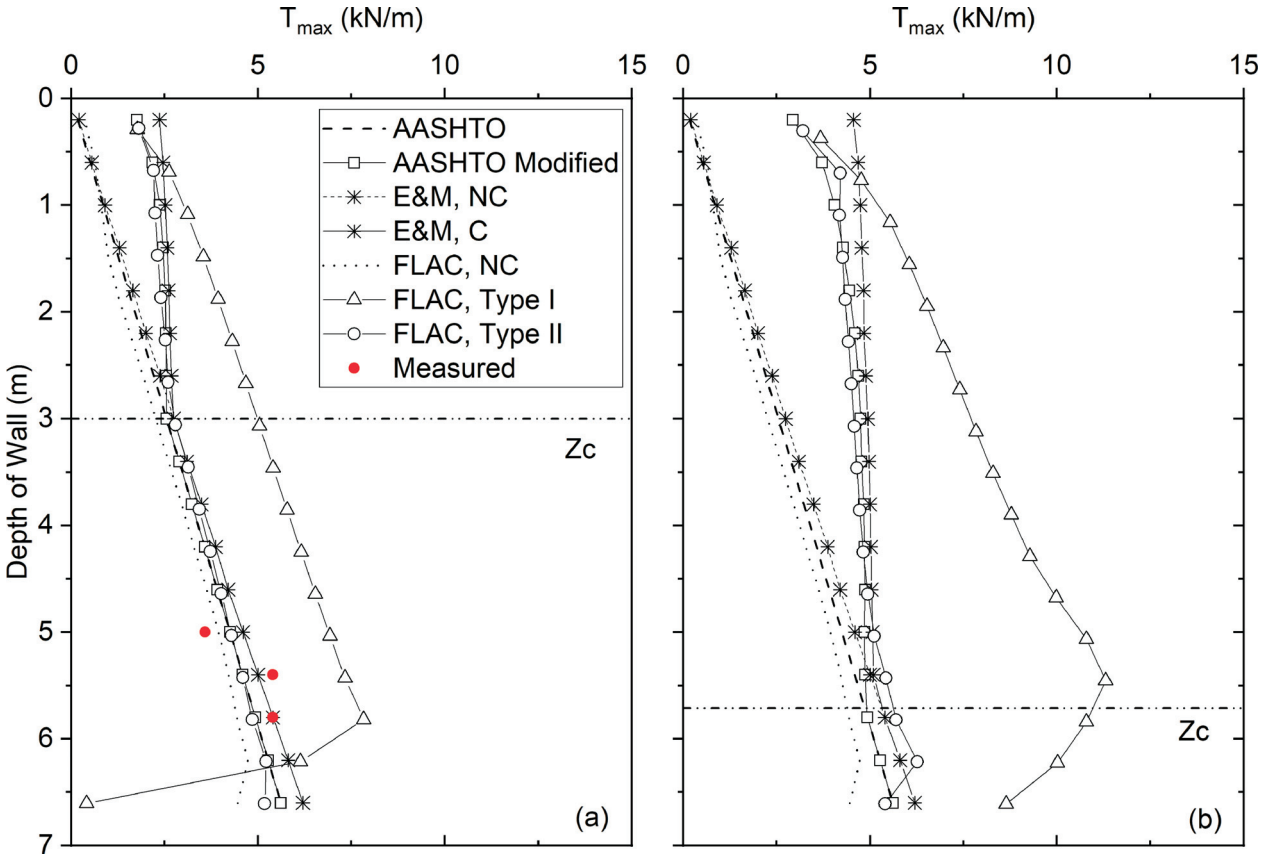

Figure 22. Depth of wall *vs.* individual values of T_{max} at the end of construction; a) $\sigma'_{ZC,i}$ = 63 kPa, and b) $\sigma'_{ZC,i}$ = 120 kPa.

two different procedures to simulate the CIS and the results of the modelling during construction and post construction were compared against the data from a full-scale GRS segmental wall built at the Royal Military College of Canada. Furthermore, the calculated values of T_{max} using two design methods have been compared to the measurements and numerically calculated T_{max} to evaluate the prediction accuracy of these methods when the value of the CIS is relevant. The main findings of this study are summarized, as follows.

The results of the experimental study highlight the importance of the compaction conditions close to the back of the facing. It is shown that when the backfill near the back of block facing is not adequately compacted, the maximum reinforcement loads, horizontal and vertical displacements of the GRS wall increase during construction and post construction. It should be noted that in the real fieldwork, on one hand, it is common to prevent operation of heavy compactors behind the facing to minimize compaction-induced outward deformation and lateral stresses against the back of the facing. On the other hand, due to inadequate compaction in this zone, the wall may present unexpected behavior as observed in the performed tests. Therefore, it may be a good specification for backfill compaction to be performed using tamper compaction in the interval of 0.5-1.0 m behind the facing and roller compaction beyond that. Tamper compaction may lead to a more similar compaction induced stress found in a typical roller compaction (Ehrlich & Mirmoradi, 2016, Mirmoradi & Ehrlich, 2018b).

Considering the compaction modelling by applying a uniform vertical stress to the top of each backfill layer, the numerical analyses significantly overestimate the measured values of the reinforcement strains, connection loads and facing displacement. When the compaction was simulated by applying a distribution load at the top and bottom of each soil layer, satisfactory agreement has been generally observed between measurements and calculated values during construction (Mirmoradi and Ehrlich, 2018a) and surcharge loading (Nascimento *et al.*, 2020).

The measured and calculated T_{max} values were compared with the AASHTO simplified, AASHTO modified and Ehrlich & Mirmoradi (2016) design methods. The Ehrlich & Mirmoradi (2016) method properly captured measured and calculated values of T_{max} whether or not CIS is applied on the backfill. The AASTHO simplified method may properly represent T_{max}, in which no CIS was assumed for a wrapped-face wall. However, the AASTHO method may underestimate T_{max} for the walls, in which a high compaction-induced stress assumed. The procedure proposed by Mirmoradi & Ehrlich (2015a) may satisfactory modify the calculated values by the AASHTO method to take into consideration the effect of CIS.

Acknowledgments

The authors greatly appreciate the funding of this study by the Brazilian Research Council, CNPq, and the Brazilian Federal Agency for Support and Evaluation of Graduate Education, CAPES. We also thank Flavio Montez and Andre Estevão Ferreira da Silva from the Huesker Company for their support, as well as Cid Almeida Dieguez for his support in performing the experiments.

References

AASHTO (2017). AASHTO LRFD bridge design specifications. 8th ed. American Association of State Highway and Transportation Officials., Washington, D.C., USA, 1780 p.

Ambauen, S.; Leshchinsky, B.; Xie, Y. & Rayamajhi, D. (2015). Service-state behavior of reinforced soil walls supporting spread footings: a parametric study using finite element analysis. Geosynth. Int., 23(3):156-170. https://doi.org/10.1680/jgein.15.00039

Bathurst, R.J.; Nernheim, A.; Walters, D.L.; Allen, T.M.; Burgess, P. & Saunders, D.D. (2009). Influence of reinforcement stiffness and compaction on the performance of four geosynthetic reinforced soil walls. Geosynth. Int., 16(1):43-59. https://doi.org/10.1680/gein.2009.16.1.43

Berg, R.; Christopher, B.R. & Samtani, N. (2009). Mechanically Stabilized Earth Walls and Reinforced Soil Slopes, Design and Construction Guidelines - FHWA-NH1-09-083 and FHWA GEC011. U.S. Department of Transportation, Federal Highway Administration, Washington, DC, 668 p.

Bernardi, M.; Collin, J.G. & Leschinsky, D. (2009). Design Manual for Segmental Retaining Walls. 3rd ed. National Concrete Masonry Association, Herndon, 281 p.

BSI (2010). BS 8006-1: Code of Practice for Strengthened/Reinforced Soils and Other Fills. BSI, London, UK, 260 p.

Campanella, R.G. & Vaid, Y.P. (1972). A simple Ko triaxial cell. Can. Geotech. J., 9(3):249-260. https://doi.org/10.1139/t72-029

Collin, J.G.; Berg, R.R. & Meyer, M.S. (2002). Segmental Retaining Wall Drainage Manual. National Concrete Masonry Association, Herndon, 96 p.

Duncan, J.M. & Seed, R.B. (1986). Compaction-induced earth pressures under Ko-conditions. J. Geotech. Engng., 112(1):1-22.

Dyer, N.R. & Milligan, G.W.E. (1984). A photoelastic investigation of the interaction of a cohesionless soil with reinforcement placed at different orientations. Proc. Int. Conf. on In-Situ Soil and Rock Reinforcement, International Society of Soil Mechanics and Geotechnical Engineering (ISSMGE), London, pp. 257-262.

Ehrlich, M. & Becker, L. (2010). Reinforced Soil Walls and Slopes: Design and Construction. Taylor & Francis, Abingdon. 118 p.

Ehrlich, M. & Mirmoradi, S.H. (2013). Evaluation of the effects of facing stiffness and toe resistance on the behavior of GRS walls. J. Geotextile Geomembr., 40(1):28-36. https://doi.org/10.1016/j.geotexmem.2013.07.012

Ehrlich, M. & Mirmoradi, S.H. (2016). A simplified working stress design method for reinforced soil walls. Géotechnique, 66(10):854-863. https://doi.org/10.1680/jgeot.16.P.010

Ehrlich, M.; Mirmoradi, S.H. & Xu D. S. (2017). A simplified working stress design method for reinforced soil walls. Geotechnique, 67(11):1029-1032. https://doi.org/10.1680/jgeot.16.D.007

Ehrlich, M.; Mirmoradi, S.H. & Saramago, R.P. (2012). Evaluation of the effect of compaction on the behavior of geosynthetic-reinforced soil walls. J. Geotextile Geomembr., 34(1):108-115. https://doi.org/10.1016/j.geotexmem.2012.05.005

Ehrlich, M. & Mitchell, J.K. (1994). Working stress design method for reinforced soil walls. J. Geot. Eng. ASCE, 120(4):625-645. https://doi.org/10.1061/(ASCE)0733-9410(1994)120:4(625)

Ehrlich, M. & Mitchell, J.K. (1995). Closure to "Working Stress Design Method for Reinforced Soil Walls" by Mauricio Ehrlich and James K. Mitchell. Journal of Geotechnical Engineering, 121(11):820-821. https://doi.org/10.1061/(ASCE)0733-9410(1995)121:11(820)

FHWA (2008). Geosynthetic design and construction guidelines, FHWA-NHI-07-092. FHWA, Washington, D.C., 592 p.

Guler, E.; Hamderi, M. & Demirkan, M.M. (2007). Numerical analysis of reinforced soil retaining wall structures with cohesive and granular backfills. Geosynth. Int., 14(6):330-345. https://doi.org/10.1680/gein.2007.14.6.330

Hatami, K. & Bathurst, R.J. (2005). Development and verification of a numerical model for the analysis of geosynthetic-reinforced soil segmental walls under working stress conditions. Canadian Geotechnical Journal, 42(4):1066-1085. https://doi.org/10.1139/t05-040

Hatami, K. & Bathurst, R.J. (2006). Numerical model for reinforced soil segmental walls under surcharge loading. J. Geotech. Geoenviron. Eng., 132(6):673-684. https://doi.org/10.1061/(ASCE)1090-0241(2006)132:6(673)

Hatami, K.; Witthoeft, A.F. & Jenkins, L.M. (2008). Influence of inadequate compaction near the facing on the construction response of wrapped-face MSE walls. Transpn. Res. Rec., 2045(1):85-94. https://doi.org/10.3141/2045-10

Holtz, R.D. & Lee, W.F. (2002). WA-RD 532.1: Internal Stability Analyses of Geosynthetic Reinforced Retaining Walls. Washington State Transportation Center (TRAC), Seattle. 466 p.

Huang, B.; Bathurst, R.J. & Hatami, K. (2009). Numerical study of reinforced soil segmental walls using three different constitutive soil models. J. Geotech. Geoenviron. Eng., 135(10):1486-1498. https://doi.org/10.1061/(ASCE)GT.1943-5606.0000092

Itasca Consulting Group (2016). FLAC - Fast Lagrangian Analysis of Continua. Version 8.0, Minneapolis.

Jaky, J. (1944). The coefficient of earth pressure at rest. J. Soc. Hungarian Archits Engrs, 78(22):355-358 (in Hungarian).

Jewell, R.A. (1980). Some Effects of Reinforcement on the Mechanical Behavior of Soils. Ph.D. Dissertation, Univ. of Cambridge, Cambridge.

Jiang, Y.; Han, J.; Zornberg, J.; Parsons, R.L.; Leshchinsky, D. & Tanyu, B. (2019). Numerical analysis of field geosynthetic-reinforced retaining walls with secondary reinforcement. Geotechnique, 69(2):122-132. https://doi.org/10.1680/jgeot.17.P.118

Koerner, R.M. & Koerner, G.R. (2013). A data base, statistics and recommendations regarding 171 failed geosynthetic reinforced mechanically stabilized earth (MSE) walls. J. Geotextile Geomembr, 40(1):20-27. https://doi.org/10.1016/j.geotexmem.2013.06.001

Koerner, R.M. & Koerner, G.R. (2018). An extended data base and recommendations regarding 320 failed geosynthetic reinforced mechanically stabilized earth (MSE) walls. J. Geotextile Geomembr., 46(6):904-912. https://doi.org/10.1016/j.geotexmem.2018.07.013

Lambe, T.W. & Whitman, R.V. (1969). Soil Mechanics, Wiley, New York, 553 p.

Liu, H.; Yang, G. & Hung, C. (2017). Analyzing reinforcement loads of vertical geosynthetic-reinforced soil walls considering toe restraint. Int. J. Geomech., 17(6):04016140. https://doi.org/10.1061/(ASCE)GM.1943-5622.0000840

Mirmoradi, S.H. & Ehrlich, M. (2014a). Modeling of the compaction-induced stresses in numerical analyses of GRS walls. Int. J. Comput. Methods (IJCM) Special Issue "Comput. Geomech.", 11(2):13422002. https://doi.org/10.1142/S0219876213420024

Mirmoradi, S.H. & Ehrlich, M. (2014b). Geosynthetic reinforced soil walls: experimental and numerical evaluation of the combined effects of facing stiffness and toe resistance on performance. Proc. 10th Int. Conf. on Geosynthetics, International Society of Soil Mechanics and Geotechnical Engineering (ISSMGE), London, v. 3, pp 2645-2652.

Mirmoradi, S.H. & Ehrlich, M. (2015a). Modeling of the compaction-induced stress on reinforced soil walls. J. Geotextile Geomembr., 43(1):82-88. https://doi.org/10.1016/j.geotexmem.2014.11.001

Mirmoradi, S.H. & Ehrlich, M. (2015b). Numerical evaluation of the behavior of GRS walls with segmental block facing under working stress conditions. ASCE J. Geotech. Geoenviron. Eng. 141(3):04014109. https://doi.org/10.1061/(ASCE)GT.1943-5606.0001235

Mirmoradi, S.H. & Ehrlich, M. (2016). Evaluation of the effect of toe restraint on GRS walls. Transp. Geotech. SI Geosynthetics in Tpt. 8(1):35-44. https://doi.org/10.1016/j.trgeo.2016.03.002

Mirmoradi, S.H. & Ehrlich, M. (2018a). Numerical simulation of compaction-induced stress for the analysis of RS walls under working conditions, J. Geotextile Geomembr., 46(3):354-365. https://doi.org/10.1016/j.geotexmem.2020.02.011

Mirmoradi, S.H. & Ehrlich, M. (2018b). Experimental evaluation of the effect of compaction near facing on the behavior of GRS walls. J. Geotextile Geomembr., 46(5):566-574. https://doi.org/10.1016/j.geotexmem.2018.04.010

Mirmoradi, S.H.; Ehrlich, M. & Dieguez, C. (2016). Evaluation of the combined effect of toe resistance and facing inclination on the behavior of GRS walls. J. Geotextile Geomembr., 44(1):287-294. https://doi.org/10.1016/j.geotexmem.2015.12.003

Nascimento, G.; Ehrlich, M. & Mirmoradi, S.H. (2020). Numerical- simulation of compaction-induced stress for the analysis of RS walls under surcharge loading. J. Geotextile Geomembr., 48(4):532-538. https://doi.org/10.1016/j.geotexmem.2020.02.011

Scotland, I.; Dixon, N.; Frost, M.; Fowmes, G. & Horgan, G. (2016). Modelling deformation during the construction of wrapped geogrid-reinforced structures. Geosynth. Int., 23(3):219-232. https://doi.org/10.1680/jgein.15.00049

Tatsuoka, F.; Uchimura, T. & Tateyama, M. (1997). Preloaded and pre-stressed reinforced soil. Soils Found., 37(3):79-94. https://doi.org/10.3208/sandf.37.3_79

Uchimura, T.; Tateyama, M.; Tanaka, I. & Tatsuoka, F. (2003). Performance of a preloaded-prestressed geogrid-reinforced soil pier for a railway bridge. Soils Found., 43(6):155-171. https://doi.org/10.3208/sandf.43.6_155

Yu, Y.; Bathurst, R.J. & Allen, T.M. (2016). Numerical modeling of the SR-18 geogrid reinforced modular block retaining walls. J. Geotech. Geoenviron. Eng., 142(5):04016003. https://doi.org/10.1061/(ASCE)GT.1943-5606.0001438

Zheng, Y. & Fox, P.J. (2017). Numerical investigation of the geosynthetic reinforced soil-integrated bridge system under static loading. J. Geotech. Geoenviron. Eng., 143(6):04017008. https://doi.org/10.1061/(ASCE)GT.1943-5606.0001665

Zheng, Y.; Fox, P.J. & McCartney, J.S. (2018). Numerical simulation of deformation and failure behavior of geosynthetic reinforced soil bridge abutments. J. Geotech. Geoenviron. Eng., 144(7):04018037. https://doi.org/10.1061/(ASCE)GT.1943-5606.0001893